Journal of Sound and Vibration 568 (2024) 117949

Contents lists available at ScienceDirect

Journal of Sound and Vibration

journal homepage: www.elsevier.com/locate/jsvi

Investigating the effect of dry-friction on damage detection tests

Giancarlo Santamato *, Massimiliano Solazzi, Antonio Frisoli

Institute of Mechanical Intelligence, Scuola Superiore Sant'Anna, via Alamanni 13b, Ghezzano, 56010, Pisa, Italy
Department of Excellence in Robotics & AI, Scuola Superiore Sant'Anna, Pisa, Italy

ARTICLE INFO

Keywords:
Dry-friction
Stick–slip transition
Damage detection

ABSTRACT

This paper investigates whether dry-friction can affect the detection of damages in the context of structural dynamics tests. The problem is confronted through a MDOF system with a single Coulomb contact and a harmonic excitation, in the presence of two damage scenarios, namely the loss of a member connectivity and a reduction of the artificial damping, also considering different locations of the frictional contact and the input excitation. In particular, we derive the trends of the damage signature with respect to the friction-over-excitation ratio. In this way, it was possible to correlate the amplitude of the damage signature to the properties of the system in the stick–slip or in the stuck regime. The investigation is also pursued through experimental tests with the same damage scenarios applying a variation of the friction ratio of one order of magnitude. Results confirm the theoretical trends and suggest that the choice of the friction ratio can also determine the appearance of false negatives for a given confidence level.

1. Introduction

Many engineering structures exhibit hysteretic behavior due to dry-friction at the connections. In particular, in linkage mechanisms, a lightweight truss frame is allowed to unfold by the presence of no-lubricated pinned joints [1]. In the context of structural dynamics characterization, these structures are inherently nonlinear in the sense that the response to external excitation is already nonlinear in the safe condition. Consequently, the modal parameters can be found dependent on the vibration amplitude based on whether the external excitation breaks the joints friction [2–5]. In this regard, extensive literature attempted to take advantage of dry friction as a source of damping [6–8] and/or vibration control [9–11], while little attention has been paid to possible damage detection implications [12].

Thereupon damage detection is often pursued by interrogating the structure under a single level of the excitation due to practical reasons, like the limited power capabilities of the exciters and the use of environmental excitation [13]. In this regard, to the best of the Authors's knowledge, it misses an adequate investigation of how a damage signature evolves with the excitation level in the presence of dry-friction. Hence the present work delves theoretically and experimentally with the open topic suggested by Worden [14], that is understanding whether frictional nonlinearity can be exploited in a damage detection sense.

Previous works proposed models of frictional oscillators, most of them adopting the Coulomb's law formulation. As authoritative examples, Den Hartog [15] and Yeh [16] found closed-form solutions to steady-state forced vibrations, but in the hypothesis of no standstill, i.e zero *stops*. On the other side, the works of Pratt [17] and Hong [18] deepened into the sticking response of a single-degree-of-freedom (DOF) system. In particular, through mixed analytical and numerical approaches, they classified the steady-state behavior in terms of the number of stops-per-cycle, and with respect to a friction ratio (Coulomb force threshold over excitation level) and a frequency ratio. The extension to multiple DOFs [19–21] was confronted experimentally [22,23] and numerically by

* Corresponding author at: Institute of Mechanical Intelligence, via Alamanni 13b, Ghezzano, 56010, Pisa, Italy.
E-mail address: giancarlo.santamato@santannapisa.it (G. Santamato).

https://doi.org/10.1016/j.jsv.2023.117949
Received 23 January 2023; Received in revised form 13 May 2023; Accepted 14 July 2023
Available online 21 July 2023

several techniques, such as time-domain [24], incremental harmonic balance [6,25], linearization [26,27], state-space shooting [28], and even analytically [29–31], under the assumption of no viscous damping and single frictional contact.

In this paper, we investigate whether dry-friction can affect the detection of damages in the context of structural dynamics tests. To this end, we utilize a MDOF model with combined Coulomb and viscous damping, subjected to harmonic excitation. Our research is focused on the global modes of linkage structures and, consequently, damage scenarios are represented by major changes, i.e. the loss of a member connectivity and a reduction of the artificial damping.

In particular, the damage signature is computed over the friction ratio from the stick–slip regimes up to a high-friction regime in which the mass in contact stays in permanent stick (*fully-stuck*). In this way, we ascertained whether the use of a low or a high friction level can enhance the detection of damage which is the main objective of this work. Besides we also analyzed the effect of the damage extent and the location of the frictional contact and the external excitation. Thus it was possible to correlate the damage signature to the properties of the system for different combinations of system parameters and friction/excitation location.

Finally, the investigation is addressed experimentally by performing structural dynamics tests on a pantograph mechanism for railway application. The aforementioned damage scenarios were replicated and the friction ratio varied over one order of magnitude. Therefore we show how, for a given damage scenario, the choice of low or high friction ratios can be detrimental because false negatives were found.

The paper is structured as follows. The formulation and the analytical expressions are derived in Section 2. In Section 3, the damage scenarios are introduced together with the choice of parameters for simulations. Section 4 shows the result of the numerical analysis of the damage signature over the friction ratio. Section 5 is devoted to the experimental structural dynamics tests. Section 6 synthesizes the work and discusses the conclusions.

2. Stick-slip and fully-stuck motion regimes in structural dynamics tests

For the sake of generality, the structure under test is represented as the n-DOF system, depicted in Fig. 1(a), consisting of a series of lumped masses m_i, springs with stiffness k_i, and viscous dampers with coefficients c_i, for $i = 1, \dots, n$.

2.1. Hypotheses

The following hypotheses are assumed:

- the system is excited on the dth mass, e.g. the *driven point* - (m_d in Fig. 1(a)) - by a harmonic load of amplitude Q_0, and frequency ω. This excitation is applied by an external exciter and it represents the system input in a structural identification sense;
- the steady-state displacement x_d of the driven-point under the external excitation is admitted to be the system output; the existence of a periodic steady-state response has been investigated by several authors [32–34] for SDOF systems while stability properties have not been explored for MDOF systems with a friction contact. Nevertheless, the numerical investigations carried out in this study have shown convergence of the response to a unique steady-state solution for most sets of parameters;
- a single Coulomb contact exists, characterized by a friction force of amplitude F that occurs on the jth mass (m_j in Fig. 1(a)). Besides the mass in contact does not coincide with the driven-point, i.e. $j \neq d$. The Coulomb friction force can be written as:

$$F(\dot{x}_j) = \begin{cases} F_0, & \dot{x}_j > 0 \\ [-\mu, \mu], & \dot{x}_j = 0 \\ -F_0, & \dot{x}_j < 0 \end{cases} \tag{1}$$

where: $\mu \geq 1$ is the ratio between the static and the kinetic values of the friction force. It should be observed that when $\dot{x}_j = 0$ the aforementioned function is mathematically undefined. Besides the value assumed in such a static condition, included between $-\mu$ and μ, ensures that the system is in equilibrium until the mass stays still. No other nonlinearities are present in the system.

2.2. Formulation of the problem

Let us introduce the stiffness coefficient k, as follows:

$$\begin{cases} k = k_{j+1}, & \text{if } j < d \\ k = k_{j-1}, & \text{if } j > d \end{cases} \tag{2}$$

The same criterion applies to the definition of the mass m, and the viscous damping coefficient c.

For the sake of simplicity, the formulation of the problem will be described with respect to a 2DOF system, represented in Fig. 1(b), where $j = 1$, $d = 2$. Moreover, the dynamic properties of the structure can be described by referring to the following non-dimensional groups ($i = 1, 2$, with $i \neq d$):

- the frequency ratio $\rho = \omega/\sqrt{k/m}$;
- the friction ratio $\beta = F_0/Q_0$
- the mass ratio $\gamma = m_1/m$;

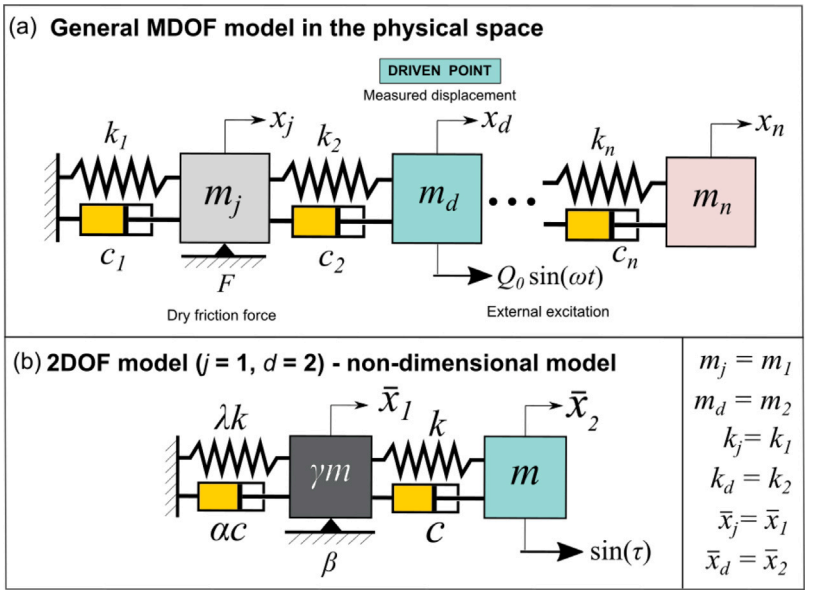

Fig. 1. (a) MDOF system for structural dynamics test with one frictional contact on the jth mass. The driven-point mass (m_d) is subjected to external harmonic excitation and its displacement is admitted to be the structural output response. (b) 2DOF reference model with non-dimensional parameters.

- the stiffness ratio $\lambda = k_1/k$;
- the damping ratio $\alpha = c_1/c$;
- the non-dimensional time $\tau = \omega t$
- the non-dimensional mass displacements: $\bar{x} = [x_1; x_2]\, k/Q_0$

Therefore, it is possible to write the governing equation of the system in the following non-dimensional matrix form:

$$\mathbf{M}\bar{\mathbf{x}}'' + \mathbf{C}\bar{\mathbf{x}}' + \mathbf{K}\bar{\mathbf{x}} + \mathbf{f} = \mathbf{q} \tag{3}$$

where:

- $\mathbf{M}$ is the mass matrix:

$$\mathbf{M} = \rho^2 \begin{bmatrix} \gamma & 0 \\ 0 & 1 \end{bmatrix} \tag{4}$$

- $\mathbf{K}$ is the stiffness matrix:

$$\mathbf{K} = \begin{bmatrix} 1+\lambda & -1 \\ -1 & 1 \end{bmatrix} \tag{5}$$

- $\mathbf{C}$ is the damping matrix:

$$\mathbf{C} = \frac{\rho c}{\sqrt{mk}} \begin{bmatrix} 1+\alpha & -1 \\ -1 & 1 \end{bmatrix} \tag{6}$$

- $\mathbf{f}$ is the Coulomb friction force vector:

$$\mathbf{f} = \beta\, \mathrm{sgn}(\bar{x}_j') \begin{bmatrix} \delta_{j1} \\ \delta_{j2} \end{bmatrix} \tag{7}$$

- $\mathbf{q}$ is the external excitation vector.

$$\mathbf{q} = \sin(\tau) \begin{bmatrix} \delta_{d1} \\ \delta_{d2} \end{bmatrix} \tag{8}$$

In Eqs. (7)–(8), the symbol δ stands for the *delta* function. The symbol ' indicates the derivative with respect to the non-dimensional time τ.

2.3. Motion regimes

Based on the state of the mass in contact, the response of the frictional system under the external excitation can be of three kinds:

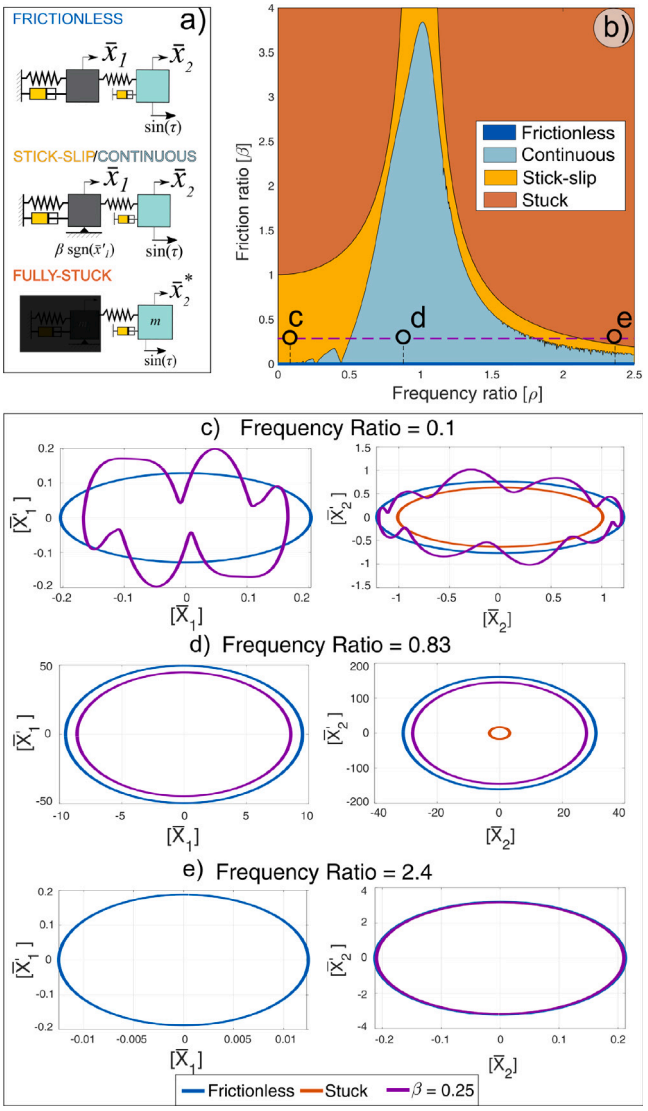

Fig. 2. (a) Schematics of a 2DOF system with frictional contact on m_1 and external excitation on m_2 in the possible frictionless, stick–slip/continuous, and fully-stuck regimes. (b) Motion regimes in the parameter space $\rho - \beta$ for $\lambda = 4$, $\gamma = 5$, $\alpha = 0$, $\xi^* = 0.5 \cdot 10^{-2}$. (c)–(d)–(e) Phase plots for the contact mass m_1 (left) and the driven-point mass m_2 (right), for different values of the frequency ratio and a friction ratio $\beta = 0.25$.

- continuous (non-sticking);
- stick–slip;
- stuck.

In terms of our formulation, the onset of each regime depends on both the frequency ρ and the friction ratio β. First, we define an auxiliary *frictionless* system for which $\beta = 0$. In this case, the system dynamics is governed by the standard modal analysis quantities [35]. Let us denote as Ω_i the natural frequencies of the frictionless system in the physical space. Hence, the natural frequencies of the non-dimensional system can be expressed as:

$$\bar{\Omega}_i = \frac{\Omega_i}{\omega} = \frac{1}{\rho}\left[\frac{(\gamma+\lambda+1) \mp \sqrt{(\gamma+\lambda+1)^2 - 4\gamma\lambda}}{2\gamma}\right]^{\frac{1}{2}} \tag{9}$$

Expressions for the modal vectors can be found in Appendix A.

In the continuous regime, at each time instant τ the sum of all the non-inertial forces on the mass in contact is above the static friction force. Consequently, the mass in contact exhibits only two stops per cycle which are located at the maximum and the minimum of the response, i.e. $\bar{x}'_j = 0$. The condition determining such a condition can be found in Appendix A.

In the stick–slip regime, the mass in contact alternates sliding and stuck phases, and for a given damping factor, a number of stops-per-cycle may occur depending on the frequency ρ and the friction ratio β [18].

Lastly, the mass in contact remains in a permanent stuck condition when the sum of all the elastic/damping forces is below the friction force. However, some of the remaining masses of the system can still exhibit a dynamic response, depending on the location of the driven-point and the friction contact. The reduced system will be referred to as *fully-stuck*.

As an example, when $j = 1$, $d = 2$, the fully-stuck configuration is represented by the system with the SDOF $\bar{x}_2^*$, while the first mass is replaced by a fixed wall, as shown in Fig. 2. Hence the response of the fully-stuck system is linear and it can be derived from standard modal analysis. It is immediate to obtain that the zero-frequency solution is $\bar{x}_2^*(\rho = 0) = 1$.

What is more, the response of the fully-stuck system will be characterized by different frequencies and different damping ratios compared to those of the frictionless system. For instance, the natural frequency of the fully-stuck mode is $\bar{\Omega}^*$:

$$\bar{\Omega}^* = \frac{\sqrt{k/m}}{\omega} = \frac{1}{\rho} \tag{10}$$

which is located between the natural frequencies of the frictionless system $\bar{\Omega}_i$ expressed by Eq. (9). Instead, the damping ratio ξ^* is:

$$\xi^* = \frac{c}{2\sqrt{m\,k}} \tag{11}$$

Therefore the condition for the arousal of the fully-stuck regime can be written as [23,29,31]:

$$k\bar{x}_j^* < \beta \tag{12}$$

When dealing with a 2DOF system, the previous Eq. (12) becomes:

$$\frac{1}{\sqrt{(1-\rho^2)^2 + 4\,\xi^{*2}\,\rho^2}} < \beta \tag{13}$$

Alternatively, for a given friction ratio, one can find the *breakaway* frequencies at which the system undergoes the transition from the stick–slip to the fully-stuck regime. Namely, the stick–slip regime holds in the frequency interval $\rho_{B_1} \le \rho \le \rho_{B_2}$ where $\rho_{B_{1,2}}$ are the breakaway frequencies, expressed by:

$$\rho_{B_1} = \begin{cases} 0, & \beta \le 1 \\ \left[1 - 2\xi^{*2} - \sqrt{\left(1-2\xi^{*2}\right)^2 - \left(1 - \frac{1}{\beta^2}\right)}\right]^{\frac{1}{2}}, & \beta > 1 \end{cases} \tag{14}$$

$$\rho_{B_2} = \left[1 - 2\xi^{*2} - \sqrt{\left(1-2\xi^{*2}\right)^2 + \left(1 - \frac{1}{\beta^2}\right)}\right]^{\frac{1}{2}} \tag{15}$$

Outside this interval, the system will stay in the fully-stuck regime. The reader should also note that for $\beta = 1$ the breakaway frequency ρ_{B_2} coincides with $\sqrt{2\left(1-2\xi^{*2}\right)}$ which tends to $\sqrt{2}$ in the case of very low damping.

Lastly, a limit friction ratio β_{lim} must be introduced:

$$\beta_{lim} = \frac{1}{2\xi^*\sqrt{1-\xi^{*2}}} \tag{16}$$

for values of β larger than β_{lim}, the mass in contact will stay stuck for all the frequencies.

In Fig. 2(b), the motion regimes of the frictional system are pictured in the plane (ρ, β), for the following set of non-dimensional parameters: $\lambda = 4$, $\gamma = 5$, $\alpha = 0$, $\xi^* = 0.5 \cdot 10^{-2}$. The phase plots of the corresponding frictionless and fully-stuck configurations are shown for different values of the frequency ratio together with the nonlinear trajectories of the mass in contact and the driven-point for $\beta = 0.25$. In particular, at low-frequency ratios, Fig. 2(c), the system is in the stick–slip regime and the frictional trajectories present a number of humps due to the stops of the mass in contact. For higher values of the frequency, the system undergoes the continuous, Fig. 2(d), and the fully-stuck regimes, Fig. 2(e). Consequently, no more stops are found and the frictional trajectories resemble the typical elliptic paths of the linear frictionless and fully-stuck solutions. In this regard, one can observe that the trajectory of the driven-point is closer to the frictionless solution when $\rho = 0.83$, while it coincides with the fully-stuck when $\rho = 2.4$.

2.4. Transmissibility function in the frequency domain

A common way to synthesize the response to harmonic excitation is to represent the time-series response in the frequency domain. However, it should be considered that due to stick–slip transition, the spectral content of the response $\bar{x}_i(\tau)$ $i = 1, \dots, n$ is in general spread over a multitude of frequency bins other than the excitation frequency ρ_d. Nonetheless, these spurious harmonics can be neglected for the purpose of this study, since we found that their amplitude is around two orders of magnitude smaller than the

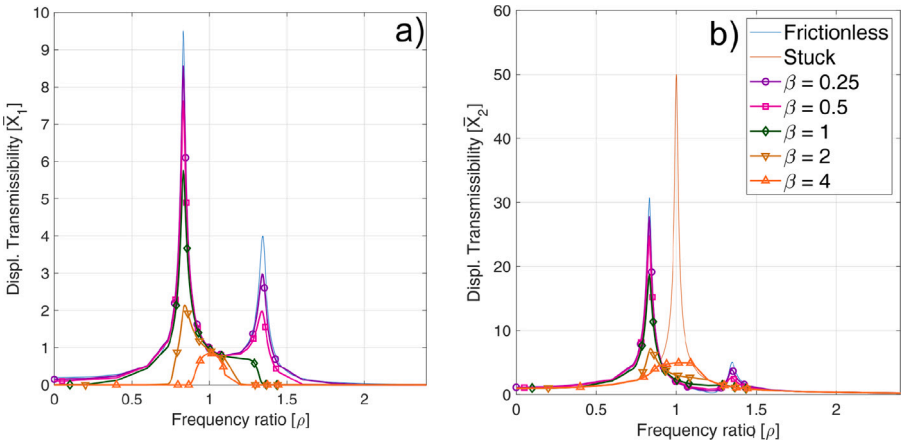

Fig. 3. Displacement transmissibility function (magnitude) for a 2DOF system with frictional contact on m_1 and external excitation on m_2 for different values of the friction ratio β ($\lambda = 4$, $\gamma = 5$, $\alpha = 0$, $\xi^* = 0.5 \cdot 10^{-2}$). (a) Response of the contact mass m_1. (b) Response of the driven-point m_2.

excitation frequency. Hence the response of the driven-point is assumed to be a mono-harmonic function at the frequency ratio ρ_d and consequently, we introduce the transmissibility function $\bar{X}_i$ as follows:

$$\bar{X}_i\left(\rho_d\right) = \mathcal{F}\left[\bar{x}_i\left(\tau\right)\right]_{\rho=\rho_d} \tag{17}$$

where $\mathcal{F}$ stands for the Fourier transform. In other words, only the principal harmonic is retained from the entire transform signal $\mathcal{F}\left[\bar{x}_i\left(\tau\right)\right]$.

The displacement transmissibilities are shown against the frequency ratio for the contact mass and the driven point, in the magnitude plot of Fig. 3(a)–(b), respectively, for the same system parameters of Fig. 2. In Fig. 3 the friction ratio ranges in $[0.25 - 0.5 - 1 - 2 - 4]$. In particular, when $\beta < 1$, the driven-point transmissibility shows two resonance peaks at the natural frequencies of the frictionless system, but the amplitude of the peaks is attenuated as β increases, due to frictional damping. For $\beta = 2$, only the first resonant peak Ω_1 is visible, but with a significant damped shape. Finally, for $\beta = 4$, no more peaks are visible, but the response shows a hump around the natural frequency of the fully-stuck system equal to 1. The properties of the breakaway frequencies highlighted by Eqs. (14)–(15) are shown by the transmissibility function of the contact mass, in Fig. 3(a). For example, when $\beta = 0.25$, the breakaway interval corresponds to $[0 - 3]$, while it reduces to $[0.75 - 1.25]$ when $\beta = 4$. As a consequence, increasing the friction ratio also increases the frequency interval in which the response of the contact mass is null (fully-stuck). As it will be shown, such a change in the shape of the response curves is crucial for structural identification analysis and fault detection.

3. Modeling of damage scenarios

In this work, the following damage scenarios have been considered:

- loss of member connectivity
- reduction of the artificial viscous damping

For each scenario, two configurations have been modeled to include the effect of different relative locations of the frictional contact and the driven-point with respect to the damage. According to the nomenclature introduced in Section 2.2, configuration 1 is defined by $j = 1$, $d = 2$, while configuration 2 is associated with $j = 2$, $d = 1$.

3.1. Loss of member connectivity

The loss of members connectivity represents one of the effects that in real structures are possibly due to damage in a bolted or a welded connection [36]. In particular, the break of a joint between two or more links generates additional DOFs which can modify the response features of a structural vibration test.

In the model of Fig. 4, the member with loss of connectivity is modeled by introducing a further spring–mass element at the end of the chain, defined through the non-dimensional stiffness ν, and the non-dimensional mass δ, which are treated as additional system parameters. A viscous damping coefficient η was also added, associated with the relative motion of the damaged mass with respect to the mass m.

In both the configurations, the masses two and three are supposed to be rigidly coupled $\left(m_2 = m(1+\delta)\right)$ when the connection is safe and hence the structure has 2DOF, i.e. $\bar{x}_2 = \bar{x}_3$. Contrariwise, in the damaged condition, the motion of the third mass becomes

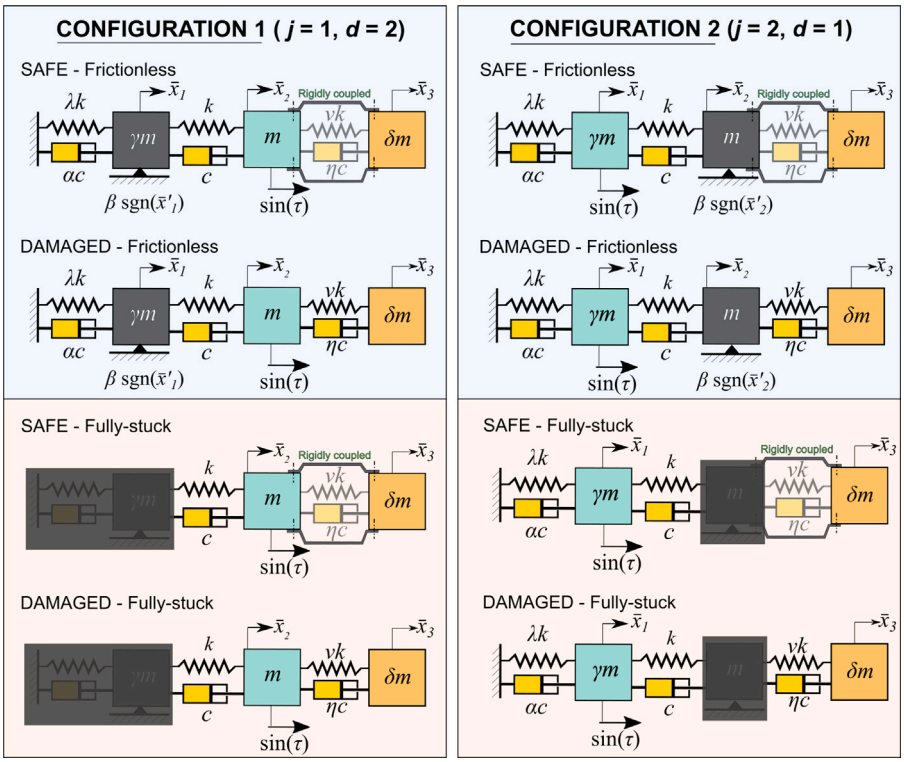

Fig. 4. Frictionless and fully-stuck configurations of a 2DOF system in the safe and the damaged condition. Damage implies the loss of a member connectivity and the emergence of a further DOF. Two possible locations of the driven-point and the frictional contact are considered (left and right).

independent of $\bar{x}_2$, and a further mode appears, or Damage Induced Mode (DIM), since the system gains a third DOF $\bar{x}_3$. Accordingly, the same system matrices for the frictionless regime can be written for both configurations:

$$\mathbf{M}^S = \rho^2 \begin{bmatrix} \gamma & 0 \\ 0 & 1+\delta \end{bmatrix} \qquad \mathbf{M}^D = \rho^2 \begin{bmatrix} \gamma & 0 & 0 \\ 0 & 1 & 0 \\ 0 & 0 & \delta \end{bmatrix} \tag{18}$$

$$\mathbf{K}^S = \begin{bmatrix} 1+\lambda & -1 \\ -1 & 1 \end{bmatrix}; \ \mathbf{K}^D = \begin{bmatrix} 1+\lambda & -1 & 0 \\ -1 & 1+\nu & -\nu \\ 0 & -\nu & \nu \end{bmatrix} \tag{19}$$

$$\mathbf{C}^S = \frac{\rho\, c}{\sqrt{m\,k}} \begin{bmatrix} 1+\alpha & -1 \\ -1 & 1 \end{bmatrix}; \ \mathbf{C}^D = \frac{\rho\, c}{\sqrt{m\,k}} \begin{bmatrix} 1+\alpha & -1 & 0 \\ -1 & 1+\eta & -\eta \\ 0 & -\eta & \eta \end{bmatrix} \tag{20}$$

where the superscripts S and D stand for the safe and the damaged condition respectively. Hence, based on these system matrices, we can expect the driven-point transmissibility $\bar{X}_d$ to be influenced by the onset of the additional DOF, at least when no friction is present, for both configurations.

Instead, a dependency on the location of the frictional contact/excitation emerges when the fully-stuck regimes are considered. Indeed in the configuration 1, we have the following system matrices:

$$\mathbf{M}^{*S} = \rho^2\,(1+\delta); \ \mathbf{M}^{*D} = \rho^2 \begin{bmatrix} 1 & 0 \\ 0 & \delta \end{bmatrix} \tag{21}$$

$$\mathbf{K}^{*S} = 1; \ \mathbf{K}^{*D} = \begin{bmatrix} 1+\nu & -\nu \\ -\nu & \nu \end{bmatrix} \tag{22}$$

$$\mathbf{C}^{*S} = \frac{\rho c}{\sqrt{m\,k}}; \ \mathbf{C}^{*D} = \frac{\rho c}{\sqrt{m\,k}} \begin{bmatrix} 1+\eta & -\eta \\ -\eta & \eta \end{bmatrix} \tag{23}$$

In other words, the mass, stiffness, and damping properties of the driven-point are altered when passing from the safe to the damaged condition. Contrariwise, in the configuration 2, the fully-stuck matrices result:

$$\mathbf{M}^{*S} = \rho^2\gamma; \ \mathbf{M}^{*D} = \rho^2 \begin{bmatrix} \gamma & 0 \\ 0 & \delta \end{bmatrix} \tag{24}$$

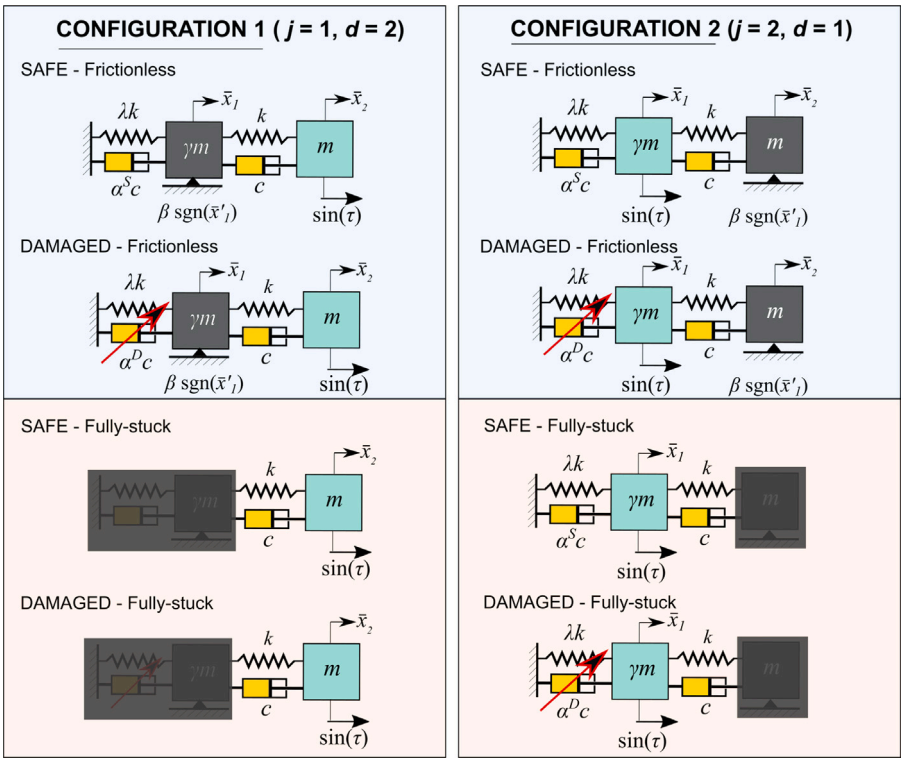

Fig. 5. Frictionless and fully-stuck configurations of a 2DOF system in the safe and the damaged condition. Damage implies the reduction of the artificial damping coefficient α located between the wall and the first mass. Two possible locations of the driven-point and the frictional contact are considered (left and right).

$$\mathbf{K}^{*^S} = 1 + \lambda; \quad \mathbf{K}^{*^D} = \begin{bmatrix} 1+\lambda & 0 \\ 0 & \nu \end{bmatrix} \tag{25}$$

$$\mathbf{C}^{*^S} = \frac{\rho c\ (1+\alpha)}{\sqrt{m\,k}}; \quad \mathbf{C}^{*^D} = \frac{\rho c}{\sqrt{m\,k}} \begin{bmatrix} 1+\alpha & 0 \\ 0 & \eta \end{bmatrix} \tag{26}$$

which shows that the coefficients of the driven-point are unchanged by the additional mass because the first and the third DOF are dynamically uncoupled. Details about how damage affects the natural frequencies, the damping ratios, and the modal shapes can be found in Appendix B.

3.2. Reduction of the artificial viscous damping

Viscous damping is a crucial mechanism for energy dissipation adopted in most structures. In particular, in linkage structures, artificial dampers are intentionally introduced to control the velocity of certain critical points [2,3,5,37]. Usually, such artificial damping is realized through hydraulic dashpots, in which the dissipating mechanism is generated by the flux of oil (or air) through designed paths. Common faults in hydraulic dampers are the break of the sealings or the sticking of the piston which in turn imply a significant variation of the viscous damping capability. In this work, we have considered the reduction of artificial damping as being a critical damage scenario for the safe operation of a structure. The correspondent model schemes for the frictionless and the fully-stuck regimes are represented in Fig. 5, where for both the configurations the artificial damper is located between the wall and the first mass γm.

The system matrices are the same as Eqs. (4)–(5)–(6) for both the safe and the damaged condition. Indeed, the arousal of the damage simply implies a variation of the dimensionless damping coefficient from the nominal value α^S to α^D. On the other side, a relevant difference emerges between configuration 1 and 2. Indeed, in configuration 1, it can be observed that the variation of the damping coefficient has no effect on the fully-stuck regime since the artificial damper is uncoupled from the driven-point due to the sticking of the contact mass. Instead, in configuration 2, the driven-point is potentially affected by the damage of the damper also in the fully-stuck regime. Details about how damage affects the natural frequencies, the damping ratios, and the modal shapes can be found in Appendix B.

3.3. Choice of parameters

Based on the previous considerations, it emerges that the difference between the transmissibility functions of the frictionless and the fully-stuck regimes plays a key role in the impact of dry-friction on damage detection. Moreover, for a given damage scenario, the extent of the damage signature on the transmissibility function depends on the values of the system parameters.

In this regard, a multitude of instances might occur, in which the introduced damage can be more or less reflected by the transmissibility function, depending on the combined effects of all the mass, stiffness, and damping coefficients of the model. What is more, no simple analytical expression can be found stating whether the frictionless and the fully-stuck response at the driven-point collide, due to the complicated expressions of the transmissibility functions when the number of DOF becomes relevant. As a consequence, the choice of parameters for simulations needs to be discussed.

Starting with the loss of member connectivity, it turns out that for high values of λ and γ, e.g. $\lambda = 10$ or $\gamma = 10$, the transmissibility function in both the frictionless and the fully-stuck regimes is mostly constant over the arousal of the additional DOF $\bar{x}_3$. Consequently, we set $\lambda = 0.1$ and $\gamma = 0.1$.

Instead, some engineering considerations can be done about the properties of the member with loss of connectivity. In this regard, we have considered that in the real structure corresponding to Fig. 4, the additional spring–mass element represents a beam that is integral with the mass m and the stiffness k in the safe condition. Hence, the stiffness ν can be expected as of the same order of magnitude as k, and thus a parametric study was carried out for two levels of the non-dimensional stiffness, $\nu = [0.5; 1.5]$. Instead, the mass δ is expected to be a fraction of the initial mass $m_2 = m(1+\delta)$. For this reason, we set $\delta = [0.05; 0.15]$. On the other side, for evaluating the effect of the damage extent, five levels of ν were considered ranging in the interval [0.375–0.75–1.5–3–6] while all the other parameters were kept constant. Since the safe condition is associated with a theoretically infinite value of this stiffness, one can conclude that the lower is ν the more the extent of the damage.

In the scenario of damping reduction, four data sets were modeled, associated with two levels of each of the non-dimensional parameters, namely: $\lambda = [0.1; 10]$ and $\gamma = [0.1; 10]$. In this way, a wide range of possible structures was considered. In the parametric study, we set $\alpha^D = 0.1\,\alpha^S$ expressing a reduction of one order of magnitude in the damping coefficient. On the other side, to evaluate the effect of the damage extent, simulations were performed for five levels of the ratio α^D/α^S ranging in the interval [0.1–0.125–0.167–0.25–0.5]. One can conclude that the damage extent is higher for the lower values of α^D/α^S.

As discussed in Section 3.2, damping is a crucial feature for most structures, and hence viscous dampers are included in the models. Nevertheless, the choice of modal damping ratios is not obvious. In this work, the viscous damping coefficients are tuned to obtain desired values of the modal damping ratios with the purpose of saving computational time. Indeed, the number of integration cycles to achieve a stationary solution of Eq. (3) significantly decreases with the damping of the system. In the same way, also the frequency resolution required to analyze the transmissibility functions is proportional to the modal damping, and this especially occurs around the resonances and the zeros frequencies, where the shape of $\bar{X}_d$ is further sharpened. Through an optimization routine, the values of c and α were found to determine a desired value of the damping ratios $\xi_{1,2}$ for both the frictionless modes of the safe system, while constraining the damping ratio of the stuck mode ξ^* above a threshold. Then, the value of η is chosen such that the damping ratio of the damage-induced mode is equal to 0.05%. The values of these damping ratios were tuned with respect to the integration routine discussed in Appendix C.

Finally, three values were considered in each dataset for the friction ratio - $\beta = [0.1; 1; 10]$ - in order to explore the effects of dry-friction over two orders of magnitude.

3.4. Numerical integration

Analytical solution to the response of a MDOF system with single Coulomb contact can be found only in the hypothesis of no damping and continuous motion regime [15,31]. Hence, integration of Eq. (3) requires in general a numerical procedure due to the presence of the nonlinear friction term $\mathbf{f}$. To this end, we opted for a direct numerical integration based on the Newmark method. When dealing with general nonlinearities, the so-called *implicit* formulation can be straightforwardly adopted since it ensures unconditional stability. Yet, iterations are required at each time instant to guess the value of the acceleration at the subsequent step.

Nonetheless, one can notice that the response of a MDOF system with a single Coulomb nonlinearity is piece-wise linear. Indeed, in each of the possible motion regimes, Eq. (3) can be linearized since the friction term disappears (stick phases) or it reduces to a constant (slip phases). Hence the *explicit* Newmark formulation [38] can be adopted throughout each phase of the motion. The discussed integration routine was coded and executed through a commercial platform for numerical computing (Matlab R2019a). Details about the treatment of the state transitions from stick–slip to fully-stuck regime, and the choice of the parameters of integration can be found in Appendix C.

4. Numerical results

This section is devoted to evaluating the impact of stick–slip and fully-stuck regimes on damage detection. The damage detection features the analysis of the displacement transmissibility function defined in Eq. (17). In particular, the error ε is evaluated over the frequency interval $[\rho_i; \rho_f]$:

$$\varepsilon = \frac{\int_{\rho_i}^{\rho_f} |\bar{X}_d^S - \bar{X}_d^D| \, d\rho}{\rho_f - \rho_i} \tag{27}$$

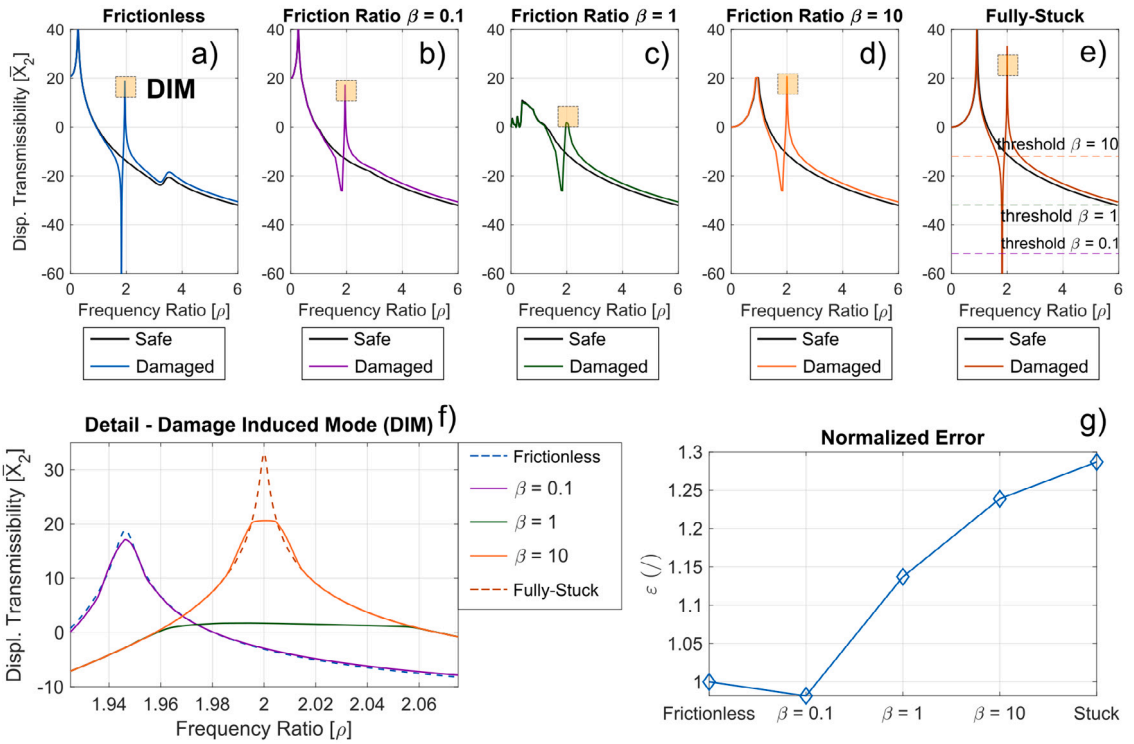

Fig. 6. (a)–(f): Safe and damaged transmissibility functions (magnitude on decibel scale) at the driven-point for a 2DOF system with a loss of member connectivity with external excitation on m_2 and frictional contact on m_1 when $\lambda = 0.1$, $\gamma = 0.1$, $\nu = 0.5$, $\delta = 0.15$ for different values of the friction ratio. (g): Normalized error function against the friction ratio.

where: $\bar{X}_d^S$ and $\bar{X}_d^D$ represent the transmissibility function of the safe system and the damaged system, respectively. For each scenario, the value of ρ_i is equal to 0, while ρ_f has been chosen to adequately include the modes of the system in the safe and the damaged conditions. Accordingly, such error is evaluated for each frictional configuration starting from the frictionless to the fully-stuck system by substituting the correspondent transmissibility functions of the safe and the damaged condition in Eq. (27). Finally, a normalized error $\bar{\varepsilon}$ is estimated by dividing the error functions obtained for the frictionless, the frictional systems, and the fully-stuck configuration by the error of the frictionless system, which is considered as a reference. Hence the analysis of the normalized error over the friction ratio provides information about the impact of the friction level on damage detection.

4.1. Loss of member connectivity

4.1.1. Configuration 1

The transmissibility functions $\bar{X}_d$ at the driven-point are shown in Fig. 6 for the frictionless, the fully-stuck and the frictional configurations ($\beta = 0.1 - 1 - 10$). Specifically, the figure is a magnitude plot on a decibel scale referred to the following set of parameters: $\lambda = 0.1$, $\gamma = 0.1$, $\nu = 0.5$, $\delta = 0.15$, $\alpha = 2.7$, $c = 0.07$, and $\eta = 0.02$.

In the safe condition, Fig. 6(a), the transmissibility function of the frictionless configuration shows a resonant peak, located around $\bar{\Omega}_1$. Instead, a damped hump is produced in the neighborhood of $\bar{\Omega}_2$. A similar damped hump profile appears in the midst of these frequencies, associated with the zero of the transmissibility function. The emergence of the damage induces as a main effect the appearance of a new resonant peak and a sharp zero.

In a similar fashion, the transmissibility function of the fully-stuck configuration, Fig. 6(e), is dominated by the resonant peak around $\bar{\Omega}_1^* = 1$ in the safe condition, while a further peak arises when damage has occurred. Besides, the thresholds associated with the friction ratios are reported with the dotted lines. The breakaway frequencies at the intersection with $\bar{X}_d^*$ define the regions of transitions from the stick–slip regimes to the fully-stuck.

When $\beta = 0.1$, Fig. 6(b), the transmissibility function collides with the frictionless solution, especially in the low-frequency region. On the other side, a high degree of similarity is observed between the transmissibility functions of the system with $\beta = 10$ and the fully-stuck configuration, Fig. 6(d). Again, the magnitude of the resonant peak is attenuated by 20 dB due to friction damping. When $\beta = 1$, Fig. 6(c), the shape of the transmissibility function is highly distorted in the low-frequency region, and no evident resonant peak associated with $\bar{\Omega}_1$ or $\bar{\Omega}_1^*$ appears.

Independently of the friction ratio, no signature of the second mode is reflected either in the safe or in the damaged condition. Instead, the resonance peak of the DIM is always reflected by the transmissibility functions although some differences can be found.

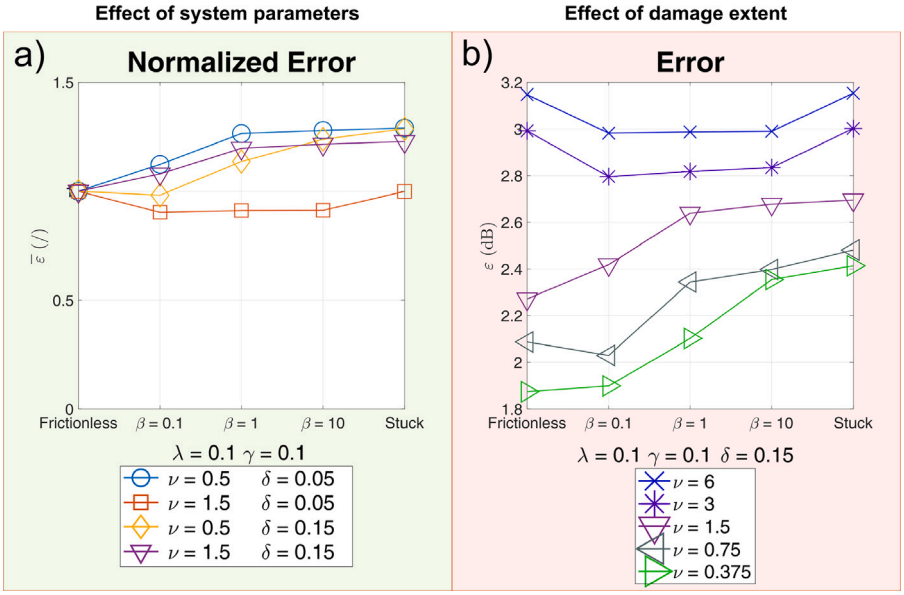

Fig. 7. Scenario loss of member connectivity, configuration 1. (a) Effect of different system parameters on the normalized error function for increasing levels of the friction ratio. (b) Effect of the damage extent on the error function (dB) for increasing values of the friction ratio.

Looking at the detail of Fig. 6(f), when $\beta = 0.1$ the peak collides with the frictionless system at a frequency equal to 1.95 and with a decreased magnitude of around 1 dB. Whereas for $\beta = 10$, the peak falls nearby the resonant peak of the fully-stuck configuration at a frequency equal to 2. Besides, compared with the fully-stuck solution, the nonlinear peak exhibits a flat profile with a decreased magnitude of 13 dB. Instead, when $\beta = 1$, the resonant peak is revealed to be more damped and attenuated compared with the other levels of the friction ratio and spread over the frequency interval 1.95–2.05.

Due to the normalization, the error function in Fig. 6(g) is equal to 1 for the frictionless configuration. A close value, equal to 0.98, is found when $\beta = 0.1$, due to the high degree of similarity with the frictionless solution. Instead, for the high friction configurations, the error function shows a progressive increase up to a value of 1.3 for the fully-stuck configuration. Such a trend indicates that damage is more emphasized when the mass in contact stays in the permanent stick regime.

For the sake of generality, simulations have been repeated for different values of the damage parameters. In particular, considering two levels for the non-dimensional stiffness ν (0.5 and 1.5) and two levels for the non-dimensional mass δ (0.05 and 0.15).

The effect of the system parameters is synthesized in Fig. 7(a), showing the normalized error function $\bar{\varepsilon}$ corresponding to each set of parameters. For all the combinations of parameters, almost the same profile of $\bar{\varepsilon}$ is found. Such a trend is correlated with the fact that increasing the friction ratio, it is reduced the damping of the DIM, (as reported in Table B.1 of Appendix B) by one order of magnitude from the frictionless to the fully-stuck configuration. This, in turn, implies a magnification of the transmissibility function for high friction values. An exception is found associated with the high value of the stiffness ν and the low value of the mass δ. In this case, the transmissibility functions of the frictionless and the fully-stuck configuration are almost coincident in both the safe and the damaged conditions. As a consequence, the error (square dot) can be considered independent of the friction ratio.

Besides, we have investigated the effect of the damage extent. For these simulations, all the parameters were kept constant, except for the stiffness of the connection ν, which was let to vary on five levels in the interval [0.375–0.75–1.5–3–6]. In order to evaluate the effect of damage extent, the results in Fig. 7(b) are shown in terms of the absolute error ε expressed in decibels. For each level of the friction ratio, the error increases with the value of ν. Such evidence is because from one set to another, the damping coefficients are constant, and only ν is changed. As a consequence, the damping ratio of the DIM increases with the stiffness ν. This, in turn, reduces the magnitude of the spike at the DIM. Besides, for the higher values of stiffness, the error reveals to be almost constant with the friction ratio as it was found in the parametric study. Otherwise, the error is emphasized by increasing β.

4.1.2. Configuration 2

The transmissibility functions $\bar{X}_d$ at the driven-point are shown in Fig. 8 for the frictionless, the fully-stuck, and the frictional configurations, and for the following set of parameters: $\lambda = 0.1$, $\gamma = 0.1$, $\nu = 0.5$, $\delta = 0.15$, $\alpha = 22$, $c = 0.01$, and $\eta = 0.17$. Again, for the frictionless system, Fig. 8(a), the emergence of the damage induces the appearance of a new resonant peak, located in the midst of the two resonant frequencies of the safe condition. Instead, no damage signature can be found in the transmissibility function of the fully-stuck configuration, shown in Fig. 8(e), since the driven-point in this configuration (DOF 1) is uncoupled with the damaged mass (DOF 3) when the contact mass achieves the stuck regime. Hence the transmissibility function of the safe and the damaged condition coincides with the response of a SDOF system. Moreover, the response of the frictional configuration resembles

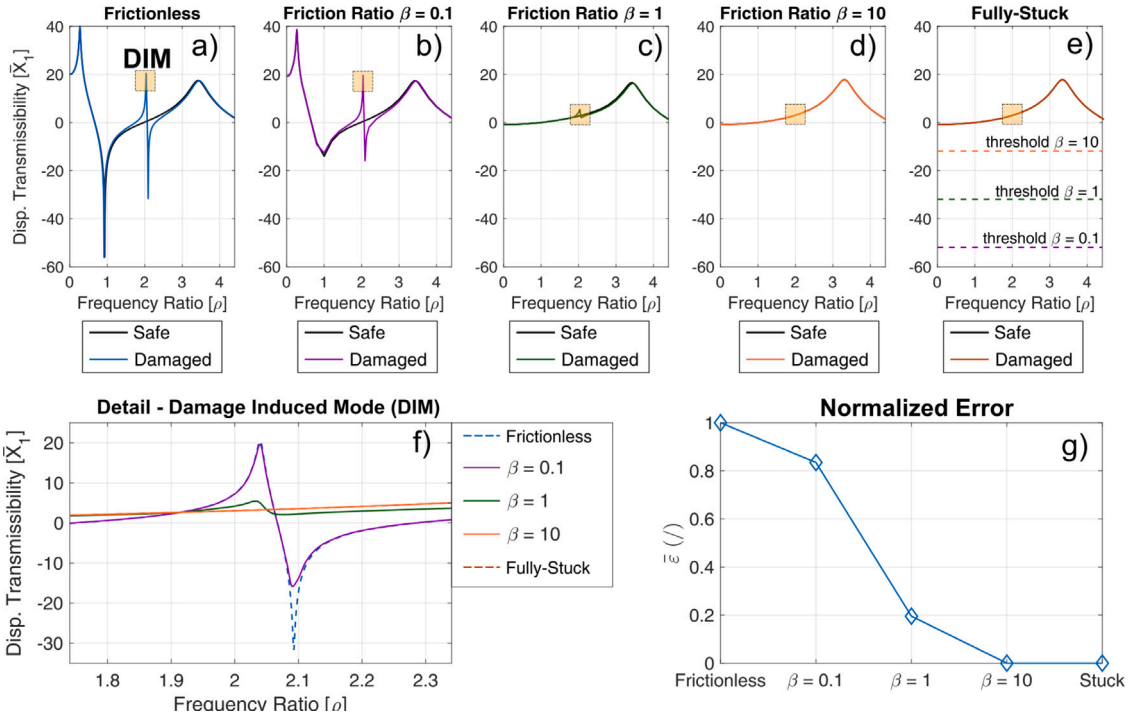

Fig. 8. (a)–(f): Safe and damaged transmissibility functions (magnitude on decibel scale) at the driven-point for a 2DOF system with a loss of member connectivity with external excitation on m_1 and frictional contact on m_2 when $\lambda = 0.1$, $\gamma = 0.1$, $\nu = 0.5$, $\delta = 0.15$ for different values of the friction ratio. (g): Normalized error function against the friction ratio.

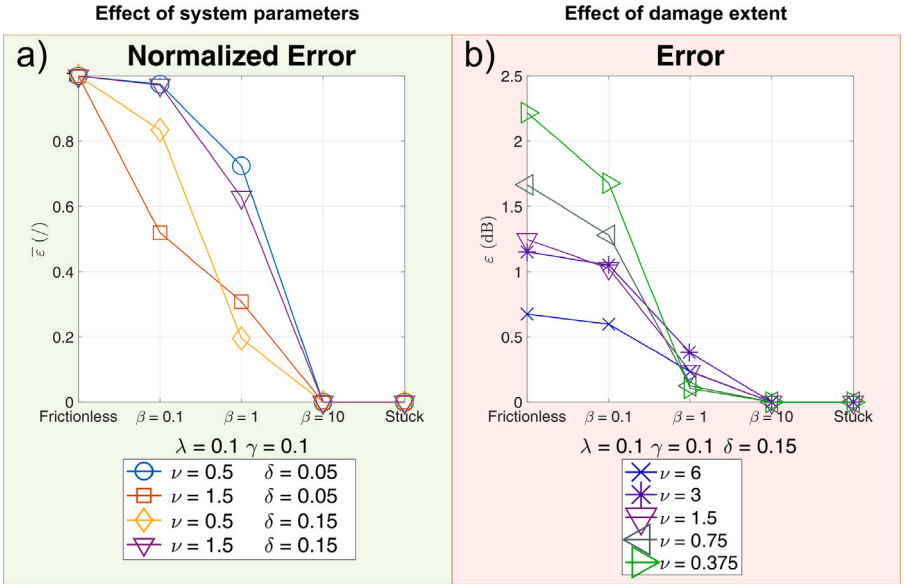

Fig. 9. Scenario loss of member connectivity, configuration 2. (a) Effect of different system parameters on the normalized error function for increasing levels of the friction ratio. (b) Effect of the damage extent on the error function (dB) for increasing values of the friction ratio.

the frictionless solution for $\beta = 0.1$, Fig. 8(b) and (f), and a difference of around 1 dB can be observed at the resonant peak of the DIM, due to frictional damping. On the other side, when $\beta = 1$ a low-amplitude peak appears due to the damage, as shown in Fig. 8(c) and in the detail of Fig. 8(f). On the other side, no damage signature is observed for $\beta = 10$, Fig. 8(d).

Consequently, the normalized error function, shown in Fig. 8(g), decreases with the friction ratio. Namely, a value of 0.82 is found when $\beta = 0.1$, which decreases to 0.2 for $\beta = 1$ and it is already zero for $\beta = 10$.

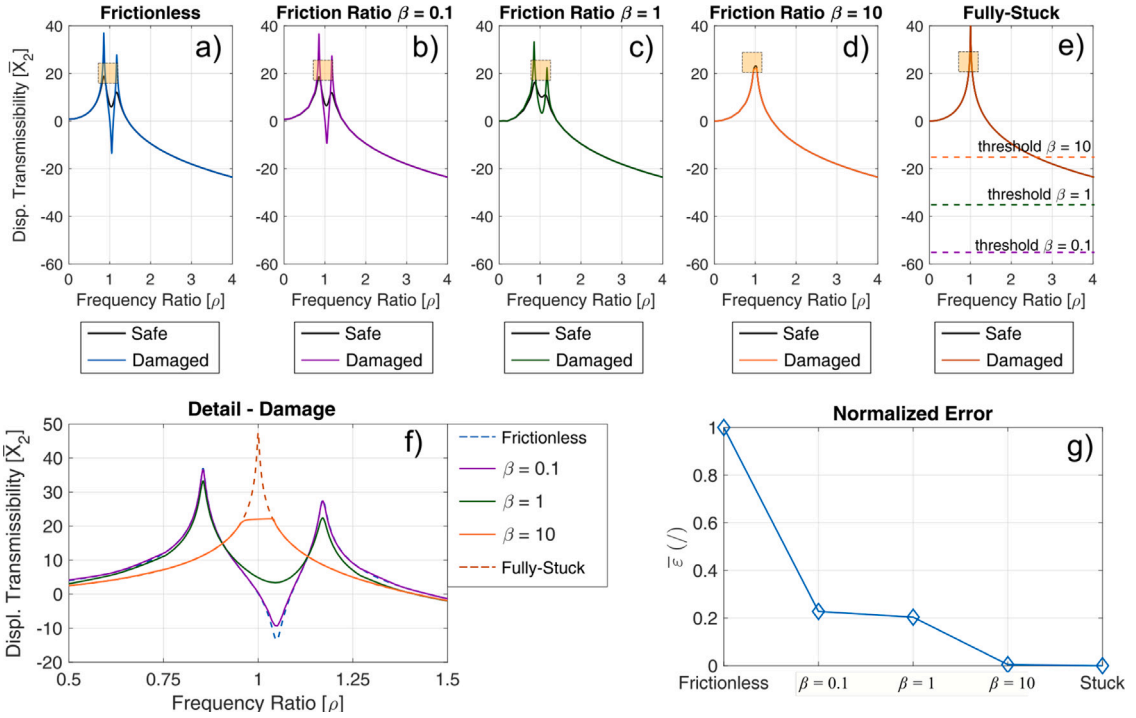

Fig. 10. (a)–(f): Safe and damaged transmissibility function (magnitude on decibel scale) at the driven-point for a 2DOF system with a reduction of artificial damping with external excitation on m_2 and frictional contact on m_1 when $\lambda = 10$, $\gamma = 10$, $\alpha^D/\alpha^S = 0.1$ for different values of the friction ratio. (g): Normalized error function against the friction ratio.

In the same criterion of the previous paragraph, simulations have been repeated for the same set of parameter values, and shown in Fig. 9(a). No significant differences are found in the behavior of the normalized error against the friction ratio despite the variations in the system parameters. Moreover, the effect of decreasing the stiffness of the connection ν is shown in 9(b). For low values of friction, the error increases with the extent of the damage and it achieves a value close to zero already for β equal to 1. For high friction regimes, the damage is not detected independently of the value of ν. Hence it is confirmed that for this configuration, the damage is enhanced by low values of the friction ratio.

4.2. Reduction of the artificial damping

4.2.1. Configuration 1

The transmissibility functions $\bar{X}_d$ at the driven-point are shown in Fig. 10 for the frictionless, the fully-stuck, and the frictional configurations and for the following set of parameters: $\lambda = 10$, $\gamma = 10$, $\alpha^S = 468$, $c = 0.03$, and $\alpha^D/\alpha^S = 0.10$.

In the safe condition, the transmissibility function of the frictionless system shows two resonant peaks, located at a frequency equal to 0.85 and 1.17, respectively, Fig. 10(a). The emergence of the damage has the only effect of increasing the magnitude of the transmissibility function around the resonant frequencies. On the other side, the fully-stuck system, Fig. 10(e), exhibits a SDOF response that is not influenced by the emergence of damage since the driven-point (DOF 2) is uncoupled with the damper that is attached on the mass in contact (DOF 1). The profile of the frictionless system is preserved by the frictional configurations when $\beta = 0.1$, and $\beta = 1$, Fig. 10(b)–(c). Instead, when $\beta = 10$, the response shows a single resonant peak whose amplitude is decreased by 25 dB with respect to the fully-stuck system, due to frictional damping, as shown in Fig. 10(f). Consequently, the normalized error function in Fig. 10(g) decreases with the friction ratio, reaching a value of 0.23 when $\beta = 0.1$ and it achieves the zero for $\beta = 10$.

The same behavior is found by changing the values of the system parameters, Fig. 11(a). An exception is found when $\lambda = 10$, $\gamma = 0.1$, as in the scenario of loss of member connectivity because the damage is not detected. What is more, again the transmissibility functions of the frictionless and the fully-stuck configurations are found to be coincident and, consequently, the error function is equal to zero, independently of the friction ratio.

The effect of damage extent has been investigated by changing the ratio α^D/α^S of the damping coefficient in the damaged and in the safe condition, and by keeping all the other parameters constant. In particular, five levels of the damage extent have been considered, ranging in the interval [0.1–0.125 - 0.167–0.25 - 0.5]. The results, shown in Fig. 11(b), confirm that the error is emphasized by low values of the friction ratio. Besides, for each level of the friction ratio, the error increases with the damage extent, although not proportionally since for higher values of the damage extent solutions tend to collide.

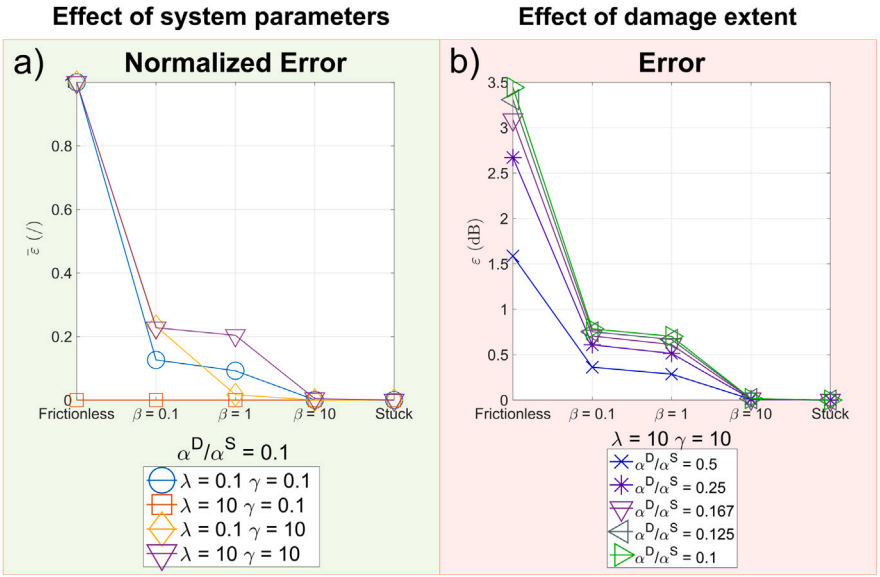

Fig. 11. Scenario reduction of artificial damping, configuration 1. (a) Effect of different parameters of the system of the normalized error function for increasing levels of the friction ratio. (b) Effect of the damage extent on the error function (dB) for increasing values of the friction ratio.

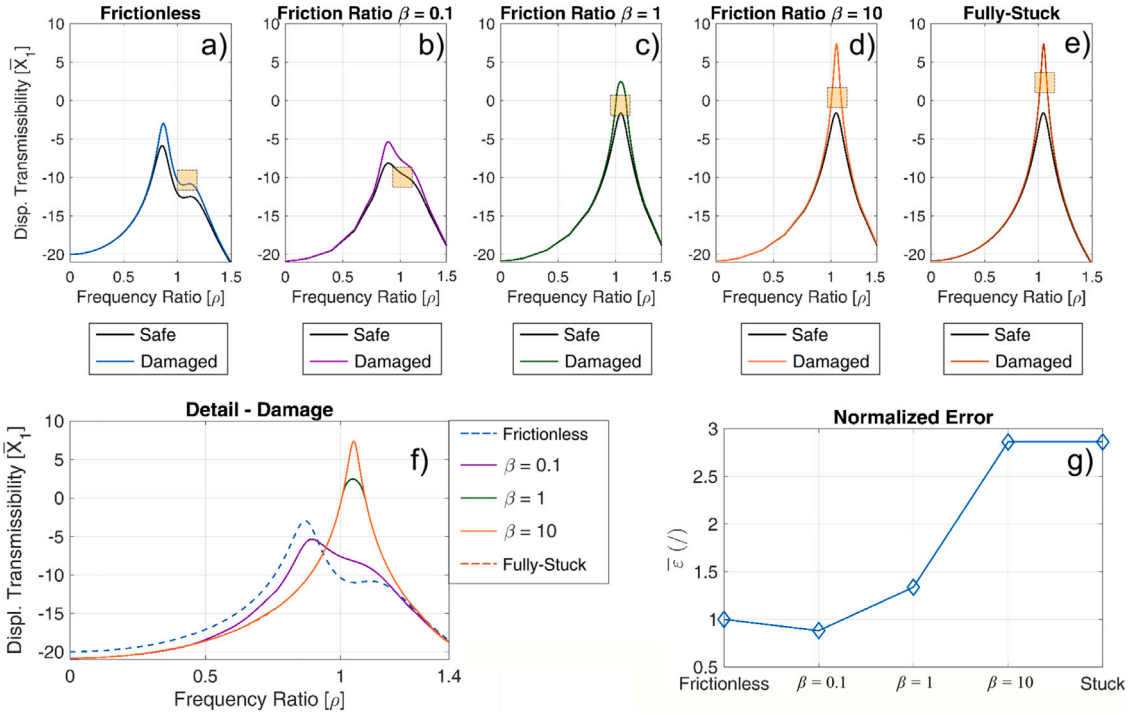

Fig. 12. (a)–(f): Safe and damaged transmissibility function (magnitude on decibel scale) at the driven-point for a 2DOF system with a reduction of artificial damping with external excitation on m_1 and frictional contact on m_2 when $\lambda = 10$, $\gamma = 10$, $\alpha^D/\alpha^S = 0.1$ for different values of the friction ratio. (g): Normalized error function against the friction ratio.

4.2.2. Configuration 2

The transmissibility functions $\bar{X}_d$ at the driven-point are shown in Fig. 12 for the frictionless, the fully-stuck, and the frictional configurations and for the following set of parameters: $\lambda = 10$, $\gamma = 10$, $\alpha^S = 2.5$, $c = 2$, and $\alpha^D/\alpha^S = 0.10$.

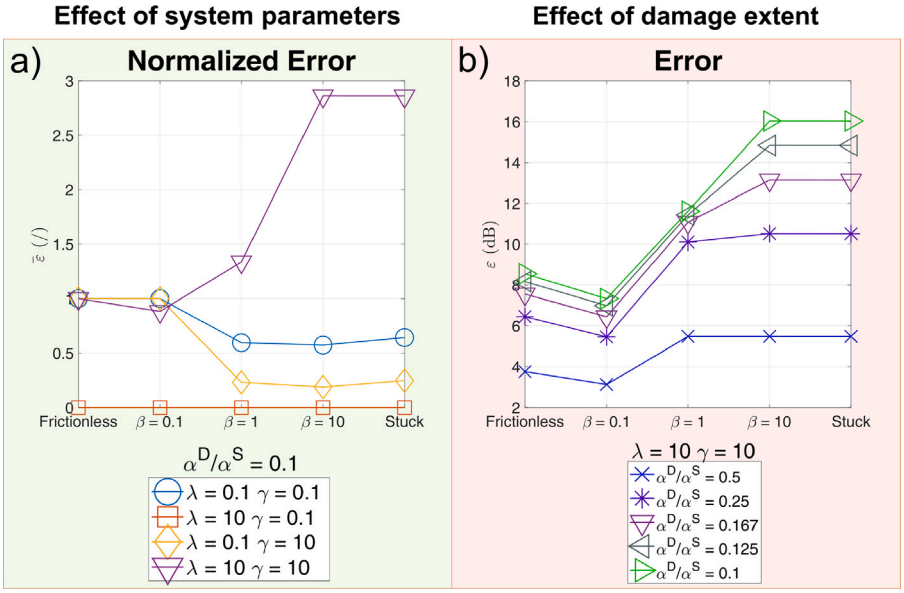

Fig. 13. Scenario reduction of artificial damping, configuration 2. (a) Effect of different system parameters on the normalized error function for increasing levels of the friction ratio. (b) Effect of the damage extent on the error function (dB) for increasing values of the friction ratio.

In the safe condition, the transmissibility function of the frictionless system shows two damped resonant peaks, Fig. 12(a). The emergence of the damage has the only effect of increasing the magnitude of the transmissibility function around those resonant frequencies. Such behavior is found also for the fully-stuck system, Fig. 12(e), which exhibits a SDOF response. Still, in this case, damage induces a sensibly higher difference between the safe and the damaged transmissibilities of around 9 dB.

The two resonant peaks of the frictionless system almost collide in a single distorted hump, when $\beta = 0.1$, Fig. 12(b) and (f). Instead, for $\beta = 1$ and $\beta = 10$, the response resembles the profile of the fully-stuck response with a single resonant peak, Fig. 12(c)–(d). Consequently, the error function shown in Fig. 12(g) increases with the friction ratio, reaching a value of 2.86 for $\beta = 10$. This evidence is correlated to the significant reduction of the damping ratio around $\bar{\Omega}^*$ in the damaged condition for the fully-stuck system.

Different behaviors are found by changing the values of the system parameters, Fig. 13(a). In particular, for low values of the stiffness λ, the damping ratio of the frictionless system becomes comparable with the fully-stuck, implying that no advantage arises from high friction regimes. Instead, for the high value of λ, the damage becomes almost negligible both in the frictionless and the fully-stuck, and consequently, it is not detected for any level of friction.

The effect of damage extent has been investigated according to the same criterion of the previous paragraph. In particular, we have investigated the case of high stiffness and mass, shown in Fig. 12. The results, shown in Fig. 13(b), confirm that the error is emphasized by increasing the friction ratio. Besides, for each level of the friction ratio, the error increases with the damage extent.

4.3. Summary of results

The outcomes of the numerical investigation can be summarized as follows:

- no optimal friction ratio exists for any frequency ratio and any kind of damage;
- the convenience of low or high friction ratio is strongly correlated with the extent to which damage modifies the transmissibilities of the frictionless and fully-stuck systems;
- when the transmissibilities of the frictionless and the fully-stuck systems coincide in the damaged condition, varying the friction ratio has no effect on damage detection. On the other side, if the error in the fully-stuck configuration exceeds the error in the frictionless, then damage detection might be enhanced by high friction ratios;
- for the high value of the stiffness coefficients λ and ν and the low value of the mass coefficients γ and δ, damage was less evident for any level of friction;
- changing the relative position of the damage and the mass in contact influences the error function. When damage is located near the driven point, detection can be enhanced by high friction regimes, but not always depending on the ratio of the fully-stuck regime with respect to the frictionless. On the other side, when the damage location and the driven point are separated by the frictional contact, we observed that the damage is emphasized by low friction ratios.

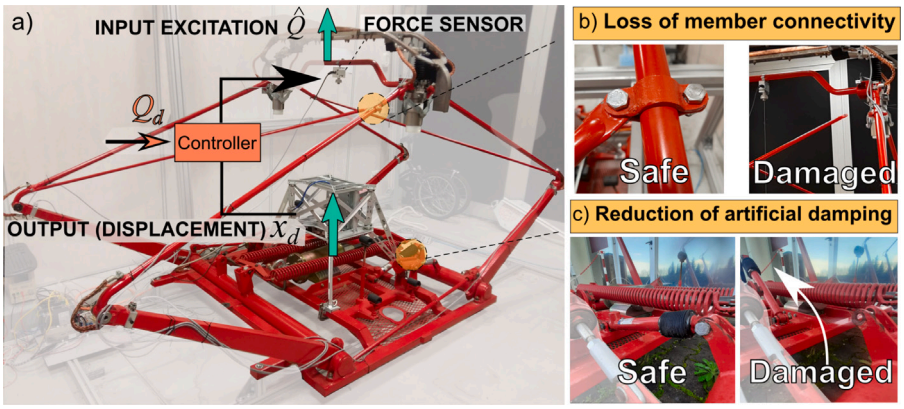

Fig. 14. Experimental setup. (a) Linkage structure (railway pantograph) in the test configuration. (b) Detail of the bolted connection that has been removed to simulate the loss of a member connectivity. (c) Detail of the hydraulic dashpot that has been removed to simulate the reduction of artificial damping.

5. Experimental investigation

With the purpose of validating the previous results, we arranged a physical setup to execute fault detection tests on a real structure by varying the level of the input excitation and evaluating the impact of dry-friction level.

5.1. Experimental setup and damage scenarios

The experimental setup, shown in Fig. 14(a), consists of:

- a real-scale railway pantograph, as an example of a structure with several dry-friction joints (base encumbrance: 1800 × 1350 mm^2; height of the pan head: 1500 mm, driven point mass: 35 kg);
- a custom exciter, endowed with a stinger actuator, able to set the level of the input excitation at a desired value within the range 1–14 N [39];
- an analog force sensor at the driven-point, embedded with a bending parallelogram amplifier, providing a resolution of $5 \cdot 10^{-3}$ N;
- a digital encoder with a resolution of $5 \cdot 10^{-2}$ mm;
- a 16-bit DAC board and a communication module based on the EtherCAT protocol.

The railway pantograph is a linkage mechanism with parallel kinematics whose end-effector is located at the top of the structure. As shown in Fig. 14(b), the experimental characterization of the pantograph is tackled through a non-parametric single-input single-output model, in which the input is the measured dynamic excitation $\hat{Q}$ applied by the exciter along the vertical direction, while the measured displacement x_d of the actuation is admitted as the output.

The input signal is generated by the controller commanding the actuation a linear chirp signal Q_d. The robot actuation applies a band-limited input excitation $\hat{Q}$ whose instantaneous amplitude $\hat{Q}_0$ is controlled by a closed-feedback loop. The objective of the control is to keep $\hat{Q}_0$ constant at each frequency bin even in the presence of disturbances (actuator friction and inertia).

For all the experiments, seven distinct values of the excitation amplitude $\hat{Q}_0$ have been considered, ranging from 1 N to 13 N. The low level was chosen according to the force resolution of the actuation. Indeed, below 1 N, some excitation is still possible but the measurements are affected by a sensibly higher noise as long as with a decrease of the input–output coherence at the resonances which drops at about 0.5, meaning poor correlation. On the other side, the high level is limited by the power of the actuation.

All the signals are measured with 1000 Hz as the sampling rate. For the purpose of limiting the complexity of the analysis, the frequency band of the input has been limited to the interval 0–10 Hz with a frequency resolution of 0.05 Hz. Fifteen repetitions of the dynamic tests have been performed in each scenario.

In the first experimental scenario, the safe pantograph was subjected to a dynamic test for the seven levels of the input excitation. Afterward, tests have been repeated with the same routine for two simulated damaged scenarios. In particular, we tampered the bolted connection of Fig. 14(c) with the aim of reproducing the loss of member connectivity that was discussed in Section 3. Besides, bolt removal has no gross effect on the kinematics due to structural redundancy since a twin connection is present on the opposite side of the mechanism. Hence the main effect of the simulated damage is introducing the bending DOF of the bar with a local and subtle alteration to structural integrity. In a second damage scenario, we removed the artificial damper by unscrewing one of its pinned connections. In this condition, the overall damping capability of the structure is expected to be reduced by 50% [40] and the only damping source is due to joints friction.

Such a linkage structure endorses several no-lubricated joints, each one experiencing a stuck or a stick–slip regime under external excitation, based on the equilibrium of the local forces. Hence several fully-stuck systems can arise during a forced vibration test.

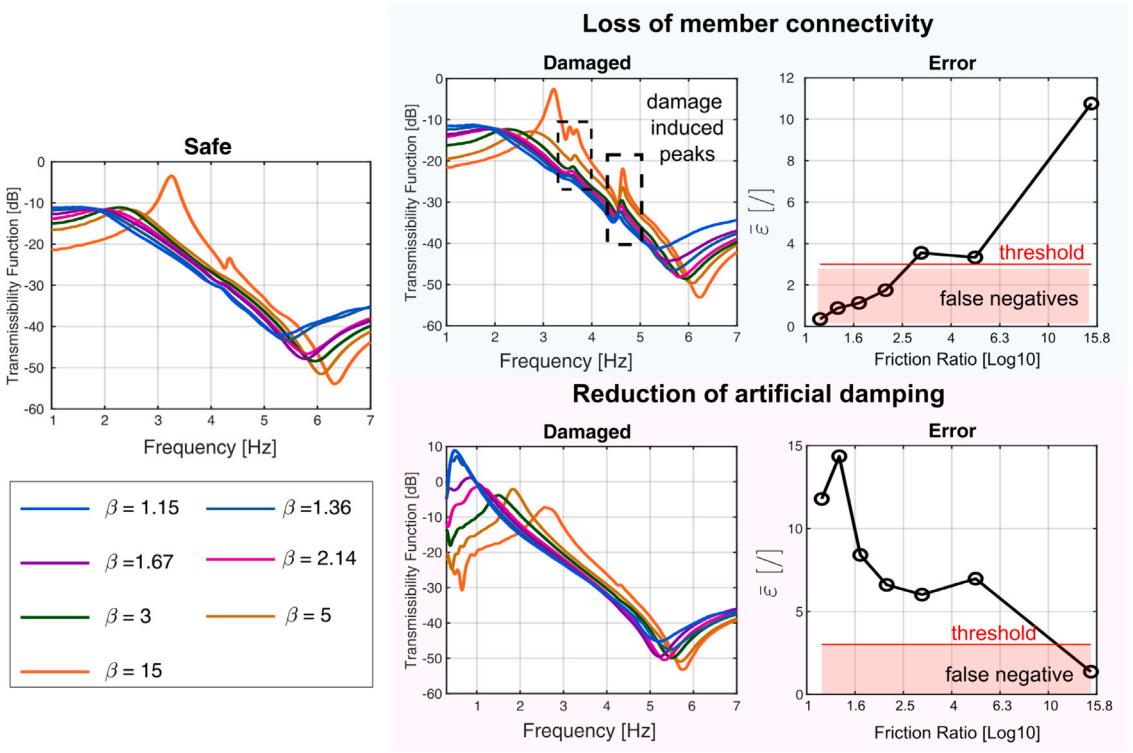

Fig. 15. Experimental transmissibility functions and correspondent error functions of the railway pantograph structure in the safe and damage scenarios for different values of the friction ratio. The threshold for the error function has been set at a confidence level of 99.7% ($z = 3$).

On the other side, the physical realization of the frictionless regime, in which all the joints are freed from friction, is not feasible, even in a laboratory environment.

Nonetheless, the investigation of dry-friction level is still possible by varying the level of the input excitation. In this case, the dry-friction at the driven-point has been estimated equal to 15 N. Consequently, the experimental friction ratio β ranges from 1.15 to 15.

5.2. Analysis of the experimental error functions

To be consistent with the formulation of Section 2, we need an experimental estimate of the transmissibility function defined in Eq. (17). Due to the homogeneous energy profile of the chirp signal $\hat{Q}_d$, we assumed the p-Welch estimate of the frequency response function, based on the input and output data record [41].

Frequency responses in the safe and damaged condition are shown in Fig. 15 for the different values of friction ratio in the interval 1–7 Hz.

In this case, no normalization of the error over the frictionless configuration is adopted. On the other side, to include statistical confidence, a hypothesis test is formulated for the error function $\bar{\varepsilon}$ as follows [42]:

$$\bar{\varepsilon} = \frac{\displaystyle\int_{f_i}^{f_f} \frac{|\bar{X}_d^S - \bar{X}_d^D|\, df}{\sigma^S \sqrt{2}}}{f_f - f_i} \leq z \tag{28}$$

where σ^S stands for the standard deviation of the experimental transmissibility function in the safe condition, f_i and f_f represent the initial and final frequency (Hz) of the considered frequency interval, and z designates a threshold defined by the standard normal distribution at a given confidence level. In this work, we assumed a confidence level of 99.7%, and thus, the threshold z is equal to 3.

In the safe condition, it emerges the presence of a dominant resonance and a residual peak that is clear for the lowest value of the friction ratio. By increasing the friction level, both peaks are progressively shifted towards lower frequencies while their amplitude gets more damped. In particular, after the first friction ratio, the second resonance is almost dampened out.

The loss of member connectivity introduces two additional resonance peaks. In the absence of the bolt, the diagonal bar behaves like a cantilever, that is free to oscillate with respect to the driven-point. First, a bending oscillation happens with a substantially

vertical component of the bar tip, at 3.6 Hz, while a mainly lateral oscillation is shown in the second mode, at 4.6 Hz. By increasing the friction level, the sharpness of the damage-induced resonances is sensibly reduced while the frequency location tends towards lower frequencies. As a consequence, the error increases with the friction ratio by a factor of 10. Moreover, for the first four levels of the friction ratio, the damage cannot be detected in a statistical sense, because the error is below the chosen threshold of statistical confidence.

The reduction of artificial damping implies a shift of the dominant peak with the frequency and an increase of the amplitude. Besides, increasing the friction ratio, the damaged transmissibility function exhibits a shifting peak (from 2.6 Hz to 0.5 Hz) and an increase of the amplitude of about 16 dB. Consequently, the error is decreased by a factor of 10, increasing the friction ratio. In this scenario, statistical confidence is always achieved, except for the highest level for the friction ratio, where the error is found below the chosen threshold of statistical confidence.

6. Conclusions

In this paper, we investigated whether the choice of a low or a high friction ratio can affect damage detection. To this purpose, we simulated numerically a MDOF system with a single Coulomb contact considering two damage scenarios: the loss of member connectivity and the reduction of artificial damping. It turns out that no optimal friction ratio exists for any frequency and any kind of damage. Besides, when damage is located near the driven point, detection might be enhanced by high friction regimes for some combinations of system parameters. On the other side, when the damage location and the driven point are separated by the frictional contact, the damage was emphasized by low friction ratios.

Experiments were also performed on a pantograph structure for railway applications confirming the trends of the error function with the friction ratio. What is more, false negatives were found for low levels of the friction ratio in the case of the loss of member connectivity, and for a high level of the friction ratio when the artificial damper had been unscrewed. Hence, as a general rule, it is worth considering the friction ratio as a parameter to be investigated during structural dynamics tests to potentially increase information about the damage occurrence.

The extension of the work in the sense of a model fitting is made interesting but also challenged by the presence of multiple dry-friction joints in real experimental structures. Consequently, multiple partial-stick modes may arise in which only a portion of all the joints stays stuck. Besides, clearance and preload fluctuations should be included because they contribute to increasing the number of possible partial-stick modes.

CRediT authorship contribution statement

Giancarlo Santamato: Conceptualization, Methodology, Simulations, Writing, Reviewing. **Massimiliano Solazzi:** Supervision, Reviewing. **Antonio Frisoli:** Supervision.

Declaration of competing interest

The authors declare that they have no known competing financial interests or personal relationships that could have appeared to influence the work reported in this paper.

Data availability

The data that has been used is confidential.

Acknowledgments

The Authors would like to thank Trenitalia SpA for the support given during the development of the research activities.

Appendix A. Complement to the analysis of the motion regimes

The mass-normalized modal shapes of the frictionless system are:

$$\psi = \frac{1}{\rho}\begin{bmatrix} \frac{1}{\sqrt{\gamma+\varphi_1^2}} & \frac{1}{\sqrt{\gamma+\varphi_2^2}} \\ \frac{\varphi_1}{\sqrt{\gamma+\varphi_1^2}} & \frac{\varphi_2}{\sqrt{\gamma+\varphi_2^2}} \end{bmatrix} \tag{A.1}$$

where:

$$\varphi_i = \frac{1}{1-\rho^2\,\bar{\Omega}_i^{\,2}} \tag{A.2}$$

It can be shown [31] that the condition of continuous motion for the system of Fig. 2 holds when:

$$\beta < \sqrt{\frac{V_j^2}{U_j^2 + [\max(S_j, \frac{\mu}{\gamma\,\rho^2})]}} \tag{A.3}$$

Table B.1
Non-dimensional modal parameters of a 2DOF system with a loss of member connectivity in the safe and damaged condition.

	Mode 1		Mode 2		DIM Mode
	SAFE	DAM	SAFE	DAM	DAM
$\bar{\Omega}$	0.27	0.27	3.43	3.45	1.95
$\bar{\Omega}^*$	0.93	0.91			2
ξ (%)	3.8	3.8	5.8	5.7	0.16
ξ^* (%)	0.52	0.48			0.05

Table B.2
Mass normalized modal shapes of a 2DOF system with a loss of member connectivity in the safe and damaged condition.

	Mode 1				Mode 2				DIM Mode	
	SAFE		DAM		SAFE		DAM		DAM	
	ψ	ψ^*	ψ	ψ^*	ψ	ψ^*	ψ	ψ^*	ψ	ψ^*
1	−0.8		0.8		−3		3		−0.4	
2	−0.9	1	0.9	0.9	0.2		−0.3		−0.3	−0.4
3			0.9	1.2			0.1		2.4	2.3

where:

$$V_j = \sum_{i=1}^{2} \psi_{ji}\,\psi_{di}\,\frac{1}{\bar{\Omega}_i^2 - 1} \tag{A.4}$$

$$U_j = \sum_{i=1}^{2} \psi_{ji}^2\,\frac{\sin(\pi\,\bar{\Omega}_i)}{\bar{\Omega}_i\,[1+\cos(\pi\,\bar{\Omega}_i)]} \tag{A.5}$$

$$S_j = \sum_{i=1}^{2} \psi_{ji}^2 \max\left[\frac{\frac{\sin(\tau\,\bar{\Omega}_i)}{\bar{\Omega}_i} + \frac{\sin(\pi\,\bar{\Omega}_i)\,[\cos(\tau)-\cos(\tau\,\bar{\Omega}_i)]}{\bar{\Omega}_i\,[1+\cos(\pi\,\bar{\Omega}_i)]}}{\sin(\tau)}\right] \tag{A.6}$$

For both the continuous and the stick–slip regime, it is possible to obtain the solution for the zero-frequency (*static value*) by neglecting the accelerations and the velocities in Eq. (3). For the system of Fig. 1 one obtains:

$$\begin{aligned} \bar{x}_1(\rho=0) &= \frac{1}{\lambda}\,(1-\beta) \\ \bar{x}_2(\rho=0) &= \frac{1}{\lambda}\,(1-\beta+\lambda) \end{aligned} \tag{A.7}$$

Appendix B. Analysis of the mode shapes and impact of the simulated damage scenarios

According to the system parameters discussed in Section 3.3, the modal parameters for the frictionless and the fully-stuck systems can be derived for each scenario and configuration, through standard modal analysis, as in Eqs. (9) and (A.1), based on the values of the system parameters in each dataset.

B.1. Loss of member connectivity - Configuration 1

For the sake of synthesis, we list in Tables B.1 and B.2 the non-dimensional modal parameters and the (undamped) mass normalized modal vectors, respectively, for $\lambda = 0.1$, $\gamma = 0.1$, $\nu = 0.5$, $\delta = 0.15$. In the safe condition, the frictionless system has two modes of vibration. In the first mode (Mode 1), the mass m_1 and the mass m_2 oscillate in phase (Eq. (A.2)) at a frequency $\bar{\Omega}_1$ equal to 0.27, and with a damping ratio of 3.8%. In the second mode (Mode 2), the oscillation occurs in phase opposition at a higher frequency equal to 3.43, and with a damping ratio of 5.8%.

As a main effect, the emergence of the damage introduces an additional mode, or Damage Induced Mode (DIM), since the system gains a third DOF. In the correspondent modal shape, the damaged mass m_3 is in opposition of phase with the driven-point, while the mass m_1 and m_2 are in phase. The corresponding natural frequency falls at 1.95, i.e. in the midst of the safe modes, and the damping ratio is 0.16%. No variation is produced in Mode 1, while a few percentage difference is observed in Mode 2 (0.58% on the frequency and 1.72% on the damping). Similar modal properties are found in the other datasets even though the numerical values of the modal properties change, especially for the frequency and the damping ratio of the DIM. For example, the DIM falls at a frequency of 5.16, i.e. above the frequencies of the safe modes when $\nu = 1.5$ and $\delta = 0.05$. Besides, slight differences occur for $\nu = 1.5$ and $\delta = 0.15$, since in the DIM the mass 1 and 2 are out-of-phase. Moreover, more significant variations are induced by the damage on Mode 2, since the natural frequency is increased by 3.8% while a decrease of 44% is produced on the damping ratio.

On the other side, in the safe condition, the fully-stuck system has one DOF, located at a frequency Ω^* equal to 1 and with a damping ratio ξ^* equal to 0.52%. As for the frictionless system, the emergence of the damage generates a new mode, but at

a frequency equal to 2 and with a damping ratio of 0.05%, i.e. one order of magnitude smaller than the damping ratio of the frictionless system. No significant variations are induced in the frequency of the first mode, while a reduction of 7% is produced on the damping ratio. Similar results are obtained for the other sets of parameters.

B.2. Loss of member connectivity - Configuration 2

In the frictionless system, similar values are found for the modal parameters and the modal vectors as in configuration 1. Contrariwise, a significant difference emerges in the properties of the fully-stuck system. First, the natural frequency of the safe condition, equal to $\sqrt{(\lambda+1)/\gamma}$ falls at a higher frequency, equal to 3.31, due to the twofold effect of the increased stiffness and a reduced mass compared to the configuration 1. The damping ratio is equal to 5.8%. Moreover, since in this configuration, masses 1 and 3 are separated by a wall, Mode 1 and the DIM are mutually independent. Therefore, the matrix of the modal vectors is the identity matrix. As a consequence, by changing the properties of the damaged member, ν and δ, the properties of Mode 1 are kept constant, while the frequency of the DIM can be straightforwardly calculated by using the SDOF formulation. As an example, for $\nu = 0.5$ and $\delta = 0.15$, one obtains a natural frequency of 1.91. It should be remembered that the damping ratio is imposed equal to 0.05%, as motivated in Section 3.3.

B.3. Reduction of the artificial damping

In both the safe and the damaged condition, two mode shapes characterize the response of the frictionless system. Namely, a low-frequency mode, in which the mass m_1 and the mass m_2 oscillate in phase, and a second mode, in which out-of-phase oscillation is found. The values of the correspondent natural frequencies depend on the choice of parameters. As an example, when $\lambda = 10$, $\gamma = 10$, one obtains: $\bar{\Omega}_1 = 0.86$ and $\bar{\Omega}_2 = 1.16$. On the other side, independently of the dataset, the damping ratios in the safe condition were set equal to 5%. The emergence of the damage implies a reduction of the damping ratios, while no effect is produced on the modal vectors and the natural frequencies. For all the dataset, both the damping ratios are found to be around 0.5% in the damaged condition, implying a reduction of one order of magnitude.

On the other side, the fully-stuck configuration is characterized by an SDOF response. In configuration 1, the natural frequency is defined by Eq. (10), while the damping ratio varies with c in each dataset, as expressed by Eq. (11). As an example, when $\lambda = 10$, $\gamma = 10$, one obtains $\xi^* = 0.20\%$. In this case, the emergence of the damage has no effect also on the damping ratio. In configuration 2, the formulas are similar, except for the fact that the stiffness is expressed by $k(\lambda+1)$, the mass is γm, and the damping coefficient is $c(1+\alpha^{S/D})$. As an example, when $\lambda = 10$, $\gamma = 10$, one obtains $\xi^* = 5\%$ in the safe condition, while for a damage extent $\alpha^D/\alpha^S = 0.1$, the damping ratio is decreased to 2% because damage also affects the fully-stuck regime.

Appendix C. Integration routine

According to the explicit Newmark formulation, given the discrete acceleration $\bar{\mathbf{x}}_\mathbf{i}''$, velocity $\bar{\mathbf{x}}_\mathbf{i}'$, and displacement $\bar{\mathbf{x}}_\mathbf{i}$, at the time instant τ_i, the solution at the subsequent time step $i+1$ can be found through the calculation of the incremental quantities:

$$\begin{aligned}\bar{\mathbf{x}}_{\mathbf{i+1}}'' &= \bar{\mathbf{x}}_\mathbf{i}'' + \Delta\bar{\mathbf{x}}_\mathbf{i}''\\ \bar{\mathbf{x}}_{\mathbf{i+1}}' &= \bar{\mathbf{x}}_\mathbf{i}' + \Delta\bar{\mathbf{x}}_\mathbf{i}'\\ \bar{\mathbf{x}}_{\mathbf{i+1}} &= \bar{\mathbf{x}}_\mathbf{i} + \Delta\bar{\mathbf{x}}_\mathbf{i}\end{aligned} \tag{C.1}$$

Such increments have the following explicit expressions [38]:

$$\begin{aligned}\Delta\bar{\mathbf{x}}_i'' &= \frac{1}{B\Delta t^2}\Delta\bar{\mathbf{x}}_i - \frac{1}{B\Delta t}\bar{\mathbf{x}}_i' - \frac{1}{2B}\bar{\mathbf{x}}_i''\\ \Delta\bar{\mathbf{x}}_i' &= \frac{\Gamma}{B\Delta t}\Delta\bar{\mathbf{x}}_i - \frac{\Gamma}{B}\bar{\mathbf{x}}_i' - \left(\frac{\Gamma}{2B}-1\right)\Delta t\,\bar{\mathbf{x}}_i''\\ \Delta\bar{\mathbf{x}}_i &= \frac{\mathbf{K} + \frac{\Gamma}{B\Delta t}\mathbf{C} + \frac{1}{B\Delta t^2}\mathbf{M}}{\Delta\mathbf{q} + \left[\frac{1}{B\Delta t}\mathbf{M} + \frac{\Gamma}{B}\mathbf{C}\right]\bar{\mathbf{x}}_i' + \left[\frac{1}{2B}\mathbf{M} + \left(\frac{\Gamma}{2B}-1\right)\Delta t\right]\bar{\mathbf{x}}_i''}\end{aligned} \tag{C.2}$$

where: $\Delta\mathbf{q} = \cos(\tau_i)$ is the incremental excitation, Δt represents the time step, while Γ and B are parameters that define the variation of acceleration over the time step. Clearly, when the integration is pursued during the fully-stuck regime, the system matrices $\mathbf{M}$, $\mathbf{C}$, and $\mathbf{K}$ in Eq. (C.2) are substituted by the corresponding matrices $\mathbf{M}^*$, $\mathbf{C}^*$, and $\mathbf{K}^*$ written for the fully-stuck configuration.

Still, checks are necessary to comply with contact state transitions. A first check is pursued at the stops, i.e. when the velocity of the mass in contact $\bar{x}_j'$ vanishes. At these time steps, the sum of all the non-inertial forces acting on m_j is compared to the friction force to guess if the system is in slip or stick. Besides, when the system is in slip and stops are excluded, it must be checked the sign of the velocity obtained by Eq. (C.2): if $\mathrm{sgn}\left[\Delta\bar{\mathbf{x}}_{i+1}'\right] \neq \mathrm{sgn}\left[\bar{\mathbf{x}}_i'\right]$, then the arousal of the stuck regime is assumed.

In our integration routine, Γ and B were imposed equal to 0.5 and 0.25 respectively: these values correspond to assuming average acceleration over the time step and they ensure unconditional stability independently of the size of the time step. However, care must be taken in the choice of Δt to ensure the accuracy of results. This is particularly crucial when the integration is carried out at low-frequency values of the excitation. In this regard, the value of the time step was set according to the frequency ratio ρ. As an example, in the scenario of Section 3.1, when $\rho \leq 0.5$ we set $\Delta t = 2\cdot10^{-4}$; otherwise: $\Delta t = 5\cdot10^{-4}$. Integration was carried on until the

response achieved steady-state. Such a condition was expressed through the energy dissipated per cycle: when the energy changed less than 5% for the last two cycles, steady-state was assumed. Integration was pursued on a number of excitation frequencies. This is crucial in terms of the spectral resolution of the transmissibility function. Moreover, the less the modal damping of the system, the higher is the frequency resolution. To this end, we adopted an average frequency resolution of 0.1 which was increased up to $0.5 \cdot 10^{-3}$ around the natural frequencies. The discussed integration routine was coded and executed through a commercial platform for numerical computing (Matlab R2019a).

References

[1] R. Plunkett, Friction damping. Damping application for vibration control, in: The Winter Annual Meeting of the ASME, 1980, pp. 65–73.
[2] J. Ting, E. Crawley, Characterization of damping of materials and structures from nanostrain levels to one thousand microstrain, AIAA J. 30 (7) (1992) 1856–1863.
[3] M.D. Ingham, E.F. Crawley, Microdynamic characterization of modal parameters for a deployable space structure, AIAA J. 39 (2) (2001) 331–338.
[4] D. Losanno, J. Londono, S. Zinno, G. Serino, Effective damping and frequencies of viscous damper braced structures considering the supports flexibility, Comput. Struct. 207 (2018) 121–131.
[5] J.Y. Yoon, D.L. Trumper, Friction microdynamics in the time and frequency domains: Tutorial on frictional hysteresis and resonance in precision motion systems, Precis. Eng. 55 (2019) 101–109.
[6] W. Dai, J. Yang, M. Wiercigroch, Vibration energy flow transmission in systems with Coulomb friction, Int. J. Mech. Sci. 214 (2022) 106932.
[7] A. Berman, W. Ducker, J. Israelachvili, Experimental and theoretical investigations of stick-slip friction mechanisms, in: Physics of Sliding Friction, Springer, 1996, pp. 51–67.
[8] A. Ferri, Friction damping and isolation systems, 1995.
[9] R. Ibrahim, Friction-induced vibration, chatter, squeal, and chaos—part I: mechanics of contact and friction, 1994.
[10] L. Gagnon, M. Morandini, G.L. Ghiringhelli, A review of friction damping modeling and testing, Arch. Appl. Mech. 90 (1) (2020) 107–126.
[11] H. Mousavi, S. Sabbagh Yazdi, M. Almohammad-Albakkar, A novel method for efficient design of frame structures equipped with nonlinear viscous dampers by using computational results of cylindrical friction damper, Aust. J. Struct. Eng. 24 (1) (2023) 50–66.
[12] A. Sadeqi, E.I. Katsanos, Nonlinear dynamic analysis and damage detection of a mass-slider system with stick–slip vibration, Nonlinear Dynam. (2023) 1–21.
[13] B. Peeters, J. Maeck, G. De Roeck, Vibration-based damage detection in civil engineering: excitation sources and temperature effects, Smart Mater. Struct. 10 (3) (2001) 518.
[14] K. Worden, C.R. Farrar, J. Haywood, M. Todd, A review of nonlinear dynamics applications to structural health monitoring, in: Structural Control and Health Monitoring: The Official Journal of the International Association for Structural Control and Monitoring and of the European Association for the Control of Structures, Vol. 15, Wiley Online Library, 2008, pp. 540–567, (4).
[15] J.D. Hartog, Forced vibrations with combined coulomb and viscous friction, in: Transaction of the American Society of Mechanical Engineering, Vol. 53, 1931, pp. 107–115.
[16] G.C. Yeh, Forced vibrations of a two-degree-of-freedom system with combined Coulomb and viscous damping, J. Acoust. Soc. Am. 39 (1) (1966) 14–24.
[17] T. Pratt, R. Williams, Non-linear analysis of stick/slip motion, J. Sound Vib. 74 (4) (1981) 531–542.
[18] H.-K. Hong, C.-S. Liu, Coulomb friction oscillator: modelling and responses to harmonic loads and base excitations, J. Sound Vib. 229 (5) (2000) 1171–1192.
[19] M. Pascal, Dynamics of coupled oscillators excited by dry friction, J. Comput. Nonlinear Dyn. 3 (3) (2008).
[20] M. Pascal, New events in stick-slip oscillators behaviour, J. Appl. Math. Mech. 75 (3) (2011) 283–288.
[21] M. Pascal, New limit cycles of dry friction oscillators under harmonic load, Nonlinear Dynam. 70 (2012) 1435–1443.
[22] X. Wang, B. Huang, R. Wang, J. Mo, H. Ouyang, Friction-induced stick-slip vibration and its experimental validation, Mech. Syst. Signal Process. 142 (2020) 106705.
[23] M. Scholl, B. Tiesler, G. Müller, Statistical evaluation of experimental and numerical data of stick–slip effects in harmonically excited systems, J. Sound Vib. 517 (2022) 116536.
[24] D. Hunt, W. Adams, T. Bock, Dynamic analysis of structures with friction forces at sliding junctures, J. Spacecr. Rockets 21 (2) (1984) 175–179.
[25] C. Pierre, A. Ferri, E. Dowell, Multi-harmonic analysis of dry friction damped systems using an incremental harmonic balance method, 1985.
[26] E.H. Dowell, The behavior of a linear, damped modal system with a non-linear spring-mass-dry friction damper system attached, J. Sound Vib. 89 (1) (1983) 65–84.
[27] S. Earles, E. Williams, A linearized analysis for frictionally damped systems, J. Sound Vib. 24 (4) (1972) 445–458.
[28] D. Yang, L. Wang, Z.-R. Lu, Periodic solution and stability analysis of dry friction system based on an alternate state-space shooting algorithm, Nonlinear Dynam. 111 (8) (2023) 7433–7458.
[29] M. Pascal, Sticking and nonsticking orbits for a two-degree-of-freedom oscillator excited by dry friction and harmonic loading, Nonlinear Dynam. 77 (1–2) (2014) 267–276.
[30] L. Marino, A. Cicirello, Multi-degree-of-freedom systems with a Coulomb friction contact: analytical boundaries of motion regimes, Nonlinear Dynam. 104 (2021) 35–63.
[31] L. Marino, A. Cicirello, Dynamic response of multi-degree-of-freedom systems with a Coulomb friction contact under harmonic excitation, Nonlinear Dynam. 106 (3) (2021) 1675–1709.
[32] S. Shaw, On the dynamic response of a system with dry friction, J. Sound Vib. 108 (2) (1986) 305–325.
[33] S. Natsiavas, Stability of piecewise linear oscillators with viscous and dry friction damping, J. Sound Vib. 217 (3) (1998) 507–522.
[34] G. Csernák, G. Stépán, S. Shaw, Sub-harmonic resonant solutions of a harmonically excited dry friction oscillator, Nonlinear Dynam. 50 (1) (2007) 93–109.
[35] L. Meirovitch, Fundamentals of Vibrations, Waveland Press, 2010.
[36] U. Dackermann, J. Li, B. Samali, Identification of member connectivity and mass changes on a two-storey framed structure using frequency response functions and artificial neural networks, J. Sound Vib. 332 (16) (2013) 3636–3653.
[37] S.L. Folkman, F.J. Redd, Gravity effects on damping of a space structure with pinned joints, J. Guid. Control Dyn. 13 (2) (1990) 228–233.
[38] A. Chopra, Dynamic of Structures. theory and Applications to Earthquake Engineering, Prentice Hall, New Jersey, 1995.
[39] G. Santamato, D. Chiaradia, M. Solazzi, A. Frisoli, A lightweight robotic device based on a micro-macro actuation concept for the inspection of railway pantograph, J. Mech. Robot. 12 (6) (2020) 061002.
[40] G. Santamato, D. Chiaradia, M. Solazzi, A. Frisoli, A lightweight robotic device for the inspection of railway pantograph, in: 2019 IEEE International Symposium on Safety, Security, and Rescue Robotics (SSRR), IEEE, 2019, pp. 284–289.
[41] J. Schoukens, T. Dobrowiecki, R. Pintelon, Parametric and nonparametric identification of linear systems in the presence of nonlinear distortions-a frequency domain approach, IEEE Trans. Automat. Control 43 (2) (1998) 176–190.
[42] F.P. Kopsaftopoulos, S.D. Fassois, Vibration based health monitoring for a lightweight truss structure: experimental assessment of several statistical time series methods, Mech. Syst. Signal Process. 24 (7) (2010) 1977–1997.